Mechanical Systems and Signal Processing 208 (2024) 111063

Contents lists available at ScienceDirect

Mechanical Systems and Signal Processing

journal homepage: www.elsevier.com/locate/ymssp

A critical evaluation of SEMM-based joint identification procedure to reduce the error propagation effects

Matteo Di Manno [a,*], Jacopo Brunetti [b], Walter D'Ambrogio [b], Annalisa Fregolent [a]

[a] Dipartimento di Ingegneria Meccanica e Aerospaziale, Università di Roma La Sapienza, Via Eudossiana, 18, Roma, 00184, Italy
[b] Dipartimento di Ingegneria Industriale e dell'Informazione e di Economia, Università degli Studi dell'Aquila, Piazzale Ernesto Pontieri, 1, Monteluco di Roio, L'Aquila, 67100, Italy

ARTICLE INFO

Communicated by M. Brake

Keywords:
Joint identification
Experimental substructuring
Substructure decoupling
System Equivalent Model Mixing
Error propagation
Monte Carlo simulation

ABSTRACT

Mechanical joints play a critical role in many engineering structures, but identifying their characteristics can be challenging, particularly when the joint interface (coupling DoFs) cannot be directly measured. In these cases, an existing iterative procedure based on the use of the System Equivalent Model Mixing (SEMM) expansion technique and substructure decoupling can be used to identify the joint properties by taking measurement on other accessible DoFs (internal DoFs). Despite the potential of this procedure, it is prone to large error propagation. In addition, in the SEMM expansion a weighted pseudo-inverse operation is needed to ensure the convergence of the iterative procedure when both coupling and internal DoFs (extended interface) are involved in the decoupling.

This paper focuses on the detection of the error sources in the process and on the definition of some strategies to limit error propagation. The use of internal DoFs only (pseudo-interface) in the decoupling is proposed. This avoids the use of coupling DoFs affected by the expansion error. Furthermore, two strategies are proposed to improve the conditioning of the procedure when using the extended interface. Both strategies are based on the Truncated Singular Values Decomposition (TSVD). It is shown that the weights clearly indicate the number of singular values to be retained in the matrices to be inverted.

The proposed improvements are validated on a laboratory benchmark. Measurements on the benchmark are performed to validate the strategies with experimental data. In addition, the Monte Carlo method is applied using noise-polluted numerical data to evaluate the potential of the proposed strategies to mitigate the error propagation in the SEMM-based joint identification procedure.

1. Introduction

Most mechanical systems are composed of different substructures connected through joints that can significantly affect the dynamic behavior of the assembled system. In most cases, the characteristics of the joint are unknown, so it is necessary to identify the dynamic behavior of the joint starting from measurements on the assembly. This process, which is known in the literature as joint identification [1–4], can be approached in the framework of dynamic substructuring, in which a complex mechanical system can be divided into several components. Each component can then be modeled separately in the physical, modal, or frequency

* Corresponding author.
E-mail addresses: matteo.dimanno@uniroma1.it (M. Di Manno), jacopo.brunetti@univaq.it (J. Brunetti), walter.dambrogio@univaq.it (W. D'Ambrogio), annalisa.fregolent@uniroma1.it (A. Fregolent).

https://doi.org/10.1016/j.ymssp.2023.111063
Received 25 May 2023; Received in revised form 16 October 2023; Accepted 18 December 2023
Available online 26 December 2023

List of the main symbols

FRF	Frequency response function matrix
IFM	Interface flexibility matrix
U	Unknown subsystem
R	Known residual subsystem
RU	Known assembled system
J	Joint subsystem
c	Coupling DoFs (also subscript in matrix notation)
r	Internal DoFs of R (also subscript in matrix notation)
u	Internal DoFs of U (also subscript in matrix notation)
m, v	Measured and validation DoFs in SEMM (also subscript in matrix notation)
$\boldsymbol{u}$	Response vector
$\boldsymbol{f}, \boldsymbol{g}$	Vectors of external and disconnection forces between subsystems
$\mathbf{B}$	Signed Boolean matrix
λ	Vector of disconnection force intensities
$\mathbf{Y}, \mathbf{Z}$	Accelerance FRF and dynamic stiffness matrices
$(\bullet)^{\text{par, ov, hyb}}$	Concerning the parent, overlay, hybrid models
$(\bullet)^{+}$	Moore–Penrose pseudo-inverse operator
$(\bullet)^{W,+}$	Weighted pseudo-inverse operator
$(\bullet)^{H}$	Hermitian (complex conjugate) operator
$\mathbf{W}$	Weighting matrix
$\mathbf{M}$	Square root of the weighting matrix
$w_{\text{m}}, w_{\text{v}}, w_{\text{c}}$	Scalar weights on the measured, validation and coupling DoFs
σ_i	ith singular value
σ	Standard deviation

domain [5]. In this way, the joint can be identified as a standalone substructure. Based on this approach, several joint identification techniques have been proposed in the literature [6–9].

Dynamic substructuring also allows for predicting the joints' dynamic effect on the assembled system. Working in the frequency domain is particularly appealing when dealing with experimental data. In the classical FRF-based substructuring (FBS) [10] introduced by Jetmundsen, each component is modeled by its frequency response function (FRF) matrix. The most straightforward application of FBS is coupling, where the dynamic behavior of the assembled system is obtained by coupling the models of the subsystems. In the Lagrange multiplier FBS (LM FBS) formulation [11], this is done by imposing compatibility and equilibrium conditions on some degrees of freedom (DoFs) that are shared between the subsystems, i.e. at the connecting (coupling) DoFs. Similarly, LM FBS allows performing decoupling [12–14], where the dynamic behavior of an unknown subsystem is identified based on the known dynamics of the assembled system and those of the other (remaining) subsystems. The decoupling can be performed by adding a fictitious substructure with an FRF matrix opposite in sign to that of the residual subsystems. In this case, the DoFs shared between the residual substructures and the assembled system, where compatibility and equilibrium can be imposed, constitute the so-called decoupling interface. However, in decoupling, the internal DoFs (not belonging to the couplings) of the residual subsystems can also be used as interface DoFs. In [15], the advantages and disadvantages of including internal DoFs in the decoupling interface are investigated in detail. In particular, the standard (coupling DoFs only) and extended (coupling and internal DoFs) interfaces are discussed. Other articles [16,17] propose the possibility of using only internal DoFs (pseudo-interface). However, measuring the FRFs of the assembled system that correspond to the coupling DoFs is still necessary.

In joint identification, the joint substructure usually has only coupling DoFs. Therefore, depending on the decoupling interface used, measurements at the coupling DoFs are required, at least for the assembled system. In applications where the joint has rotational DoFs, or when the joint interface is inaccessible for measurements, the coupling DoFs cannot be measured directly. Additional techniques are required to obtain this information. One useful technique is the Virtual Point Transformation (VPT) [18], which reduces the dynamics of the interface region to that of some virtual points, having both translational and rotational DoFs, using local rigid Interface Deformation Modes (IDMs). When the interface is deformable, one option is to extend the VPT reduction basis with flexible interface deformation modes [19]. Another possibility is using expansion techniques, defined in both the modal [20,21] and frequency domain [22]. The System Equivalent Model Mixing (SEMM) expansion technique was first formulated in the FBS framework [22], and then in the modal domain [23]. It combines numerical and experimental models of a component to obtain the FRFs at unmeasured DoFs, starting from the FRFs measured at accessible DoFs. In [24], the SEMM expansion technique is implemented in an iterative coupling–decoupling procedure useful for joint identification in applications where the joint interface cannot be measured. The procedure is validated by identifying the joint in a numerical truss structure. In [25], a similar iterative procedure is adopted to identify the inaccessible dove-tail joint in a bladed disk structure using experimental measurements. In this

application, the SEMM is combined with the VPT to obtain information at the joint interface. In the decoupling step, an extended interface is used. Weighted pseudo-inversion is used to perform matrix inversions in the SEMM expansion of the assembled system. In this process, the coupling DoFs c are given a significantly larger weight than the others. This weighting is needed to achieve convergence in a small number of iterations. However, the results obtained are highly affected by spurious peaks, as the weights assigned in this way affect the conditioning of the SEMM matrices to be inverted and consequently that of the IFM. An approach to improve the results is proposed in [26]. In particular, different combinations of the experimental FRFs are used to generate many updated models of the subsystems component. The Frequency Response Assurance Criteria (FRAC) is then used to evaluate the influence of different measurements on the result of the expansion, and the lowest correlated measuring channels, which exhibit a value of the FRAC under a given threshold, are filtered out. Even though this approach is able to improve the results of the joint identification, it does not limit the error propagation in the procedure.

This work highlights the sources of error propagation in the iterative joint identification procedure used in [25]. These sources are hidden in the matrix inversion in the SEMM expansion, which provides information at the unmeasured coupling DoFs, and in the decoupling step which separates the dynamics of the joint. The use of a pseudo-interface in the decoupling step is proposed. This avoids the propagation of the expansion error, which is not present in the internal DoFs. In addition, the possible advantages of using a pseudo interface are discussed by comparing the pseudo and extended interfaces when unitary weights are assigned to all DoFs in the weighted pseudo-inversions employed in the SEMM expansion of the assembled system. A technique based on fitting the identified joint's dynamic stiffness is proposed to filter out the spurious peaks in the solution. Moreover, the effects on the conditioning of the weighting procedure in SEMM expansion introduced in [25] are investigated in detail. Two strategies, based on the use of the Truncated Singular Values Decomposition (TSVD), are proposed to improve the results of this solution. In both strategies, the exact number of singular values to be truncated is related to the number of coupling DoFs of the system. The joint connecting two beams in a benchmark structure is identified using the proposed joint identification improvements. The joint is designed to be tested separately for validation purposes. The identification is carried out using both numerical data and experimental measurements. Measurements on the benchmark structure are performed to assess the effectiveness and robustness of the proposed strategies to the noise present in the experimental data. Furthermore, the Monte Carlo method is applied using noise-polluted numerical data to evaluate the uncertainty propagation of the iterative SEMM-based joint identification procedure, when employing the proposed strategies to improve quality of the solution.

The paper is organized as follows. Section 2 introduces the theoretical background, including substructure decoupling and SEMM, together with the joint identification procedure. In Section 3, the sources of error propagation in the solution, when using pseudo or extended interfaces, are highlighted and discussed in detail. Two methods are suggested in Section 4 to reduce the error propagation in the procedure. In Section 5, the effects of the weighting in the SEMM on the conditioning of the procedure are analyzed, and two strategies are proposed to improve the results. Section 6 presents the results, with different strategies, obtained with noise-free numerical data of the benchmark. In Section 7, the results obtained using experimental measurements are presented. Finally, in Section 8 the results of the Monte Carlo simulations are presented and discussed.

2. Theoretical background

In this Section, the methods used to obtain the Frequency Response Functions (FRFs) of the joint are described. In particular, the theory of substructure decoupling (Section 2.1) and the SEMM method (Sections 2.2) are recalled and fitted to the joint identification procedure, which is outlined in Section 2.3.

2.1. Substructure decoupling

Substructure decoupling [16,17] allows for the identification of the dynamic behavior of an unknown substructure U (N_U DoFs) starting from the known assembled system RU and from the known information about the residual substructure R (N_R DoFs). The unknown substructure U and the residual substructure R are connected through a set of coupling DoFs that are located on the common boundary at each side of the interface. The DoFs of the assembled system RU can be partitioned into coupling DoFs (c), internal DoFs (u) of substructure U, internal DoFs (r) of substructure R. In direct decoupling, the unknown substructure U is identified by adding to the assembled system RU a fictitious substructure with an FRF opposite in sign to that of the residual subsystem R. The equations of motion of the assembled substructure RU and of the negative substructure can be written as:

$$\boldsymbol{u} = \mathbf{Y}(\boldsymbol{f} + \boldsymbol{g}) \tag{1}$$

with

$$\mathbf{Y} = \begin{bmatrix} \mathbf{Y}^{\mathrm{RU}} & \\ & -\mathbf{Y}^{\mathrm{R}} \end{bmatrix}, \quad \boldsymbol{u} = \begin{Bmatrix} \boldsymbol{u}^{\mathrm{RU}} \\ \boldsymbol{u}^{\mathrm{R}} \end{Bmatrix}, \quad \boldsymbol{f} = \begin{Bmatrix} \boldsymbol{f}^{\mathrm{RU}} \\ \boldsymbol{f}^{\mathrm{R}} \end{Bmatrix}, \quad \boldsymbol{g} = \begin{Bmatrix} \boldsymbol{g}^{\mathrm{RU}} \\ \boldsymbol{g}^{\mathrm{R}} \end{Bmatrix} \tag{2}$$

where $\boldsymbol{u}$ is the response vector, $\boldsymbol{f}$ is the external force vector, $\boldsymbol{g}$ is the vector of connecting forces between subsystems and $\mathbf{Y}$ is the FRF matrix.

To decouple the substructures, compatibility and equilibrium conditions must be satisfied at the interface between the assembled structure RU and the negative residual substructure. The interface can include both the coupling DoFs between substructures U and R and all the internal DoFs of substructure R. Note that the number of interface DoFs must be greater than or equal to the number of coupling DoFs c. As explained in [15], four possible types of interfaces can be used:

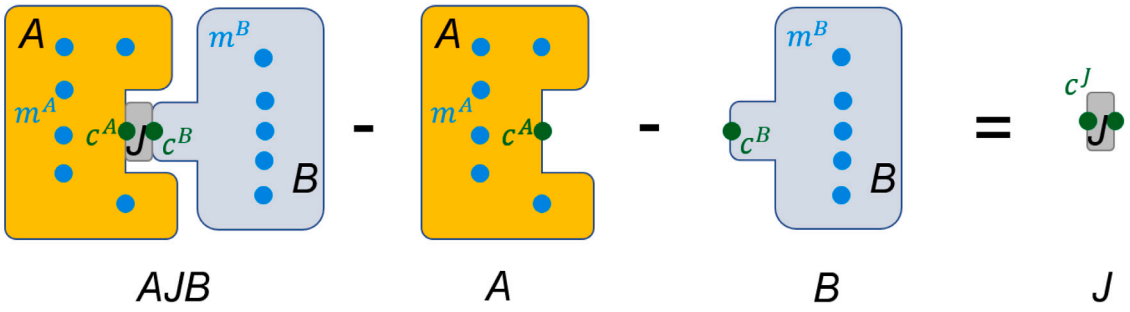

Fig. 1. Joint identification through direct decoupling. The unknown subsystem J has only coupling DoFs c.

- standard interface, including only the coupling DoFs (c) between subsystems U and R;
- extended interface, also including a subset of internal DoFs ($i \subseteq r$) of subsystem R;
- mixed interface, including subsets of coupling DoFs ($d \subset c$) and internal DoFs ($i \subset r$);
- pseudo-interface, including only internal DoFs ($i \subseteq r$) of subsystem R.

The compatibility condition at the interface DoFs implies that any pair of matching DoFs u_l^{RU} and u_n^R, i.e., DoF l on substructure RU and DoF n on substructure R, have the same displacement, that is $u_l^{RU} - u_n^R = 0$. This condition can be generally expressed by introducing the signed boolean matrix $\mathbf{B}$:

$$\mathbf{B}\boldsymbol{u} = \mathbf{0} \tag{3}$$

The equilibrium condition states that for any pair of interface DoFs, the interface forces must be equal and opposite in sign, i.e., $g_l^{RU} + g_n^R = 0$. Using the dual assembly, equilibrium is satisfied exactly by defining a unique set of disconnection force intensities λ [12,13]:

$$\mathbf{B}^T\lambda = -\boldsymbol{g} \tag{4}$$

By substituting the interface forces $\boldsymbol{g}$ from Eq. (4) into Eq. (1), the following system of equations is obtained:

$$\begin{cases} \boldsymbol{u} = \mathbf{Y}(\boldsymbol{f} - \mathbf{B}^T\lambda) \\ \mathbf{B}\boldsymbol{u} = \mathbf{0} \end{cases} \tag{5}$$

By premultiplying $\mathbf{B}$ the first line of Eq. (5), it is possible to eliminate λ and obtain the single line equation:

$$\boldsymbol{u} = \bar{\mathbf{Y}}\boldsymbol{f} \tag{6}$$

in which $\bar{\mathbf{Y}}$ (or better, a submatrix of $\bar{\mathbf{Y}}$) is the frequency response function of the unknown subsystem:

$$\bar{\mathbf{Y}} = \mathbf{Y} - \mathbf{Y}\mathbf{B}^T(\mathbf{B}\mathbf{Y}\mathbf{B}^T)^{-1}\mathbf{B}\mathbf{Y} \tag{7}$$

It is important to note that the identified FRF matrix $\bar{\mathbf{Y}}$, has the same dimensions of $\mathbf{Y}$ and some rows and columns are redundant. It is common practice to consider only those elements in the upper left block that are associated with the assembled system in the matrix $\mathbf{Y}$ (defined in Eq. (2)). Moreover, the identified FRF matrix $\bar{\mathbf{Y}}$, contains some meaningless rows and columns, those associated with the internal DoFs r, which obviously does not belong to U. Therefore, only the elements of $\bar{\mathbf{Y}}$ that correspond to the DoFs u and c should be retained. The term $\mathbf{B}\mathbf{Y}\mathbf{B}^T$ in Eq. (7) is the Interface Flexibility Matrix (IFM) that depends on the selected interface. Since this matrix has to be inverted, care must be taken if it is ill-conditioned to limit the error propagation in the solution. Note that to find the FRFs of subsystem U at a subset of coupling DoFs c and/or internal DoFs u, it is necessary to measure these DoFs in the whole system RU.

Direct decoupling can be used for joint identification. In this case, the joint J is considered as the independent unknown subsystem U with given mass and stiffness properties that connects two subsystems A and B. The residual subsystem R becomes:

$$\mathbf{Y}^{\mathrm{R}} = \begin{bmatrix} \mathbf{Y}^{\mathrm{A}} & \\ & \mathbf{Y}^{\mathrm{B}} \end{bmatrix} \tag{8}$$

The dynamic behavior of the joint J can be obtained by removing the dynamics of substructures A and B from the dynamic behavior of the assembled structure AJB, as shown in Fig. 1. It can be noted that the unknown subsystem J is defined only on the set of coupling DoFs c. When these coupling DoFs are not accessible for measurements in the whole system AJB, expansion techniques [20–23] allows obtaining the corresponding FRFs from information contained in the internal DoFs of the system AJB.

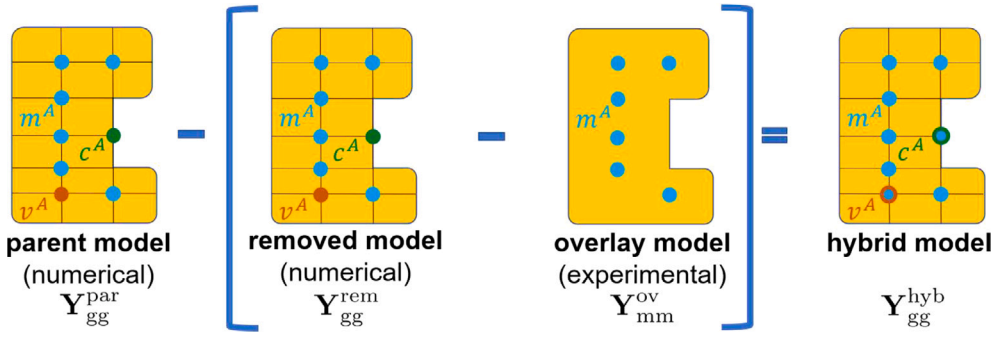

Fig. 2. The Extended SEMM expansion results from two successive decouplings that use different models of the same component. In the first decoupling, the experimental overlay model is decoupled from the numerical removed model. The resulting model is then decoupled from the numerical parent model.

2.2. System equivalent model mixing

SEMM [22] is a technique developed in the frequency-based substructuring frame to expand the information measured at a set of accessible DoFs m of a component on a set of inaccessible DoFs, in this case the coupling DoFs c, only appearing in the associate numerical model. The expansion is also performed on a set of accessible DoFs v to validate the effectiveness of the process. For this purpose, the expanded dynamics at DoFs v are compared with the corresponding experimental ones. In the end, the considered component is described by a hybrid model in which the FRFs of inaccessible DoFs are available.

The different models involved in the expansion process are described below:

- *parent model* $\mathbf{Y}^{\text{par}}$: the numerical model of the component defined on the global set of DoFs $g = m \cup v \cup c$;
- *overlay model* $\mathbf{Y}^{\text{ov}}$: the experimental model of the component obtained by measuring and exciting on the measurement DoFs m

$$\mathbf{Y}^{\text{ov}} = \mathbf{Y}^{\text{ov}}_{\text{mm}} \tag{9}$$

- *removed model* $\mathbf{Y}^{\text{rem}}$: a numerical condensed form of the parent model to the measured DoFs. In the so-called "Extended SEMM" [22] used in this work,[1] the removed model is defined on the global set of DoFs g and coincides with the parent model:

$$\mathbf{Y}^{\text{rem}} = \mathbf{Y}^{\text{rem}}_{\text{gg}} = \mathbf{Y}^{\text{par}}_{\text{gg}} \tag{10}$$

- *hybrid model* $\mathbf{Y}^{\text{hyb}}$: the resulting model. This is defined on the same DoFs of the parent model. For the Extended SEMM equation, specified for the global set of DoFs g [25], it is:

$$\mathbf{Y}^{\text{hyb}} = \mathbf{Y}^{\text{par}}_{\text{gg}} - \mathbf{Y}^{\text{par}}_{\text{gg}}(\mathbf{Y}^{\text{par}}_{\text{mg}})^{+}\mathbf{Y}^{\text{par}}_{\text{mm}}(\mathbf{Y}^{\text{par}}_{\text{gm}})^{+}\mathbf{Y}^{\text{par}}_{\text{gg}} + \mathbf{Y}^{\text{par}}_{\text{gg}}(\mathbf{Y}^{\text{par}}_{\text{mg}})^{+}\mathbf{Y}^{\text{ov}}_{\text{mm}}(\mathbf{Y}^{\text{par}}_{\text{gm}})^{+}\mathbf{Y}^{\text{par}}_{\text{gg}} \tag{11}$$

The Extended SEMM single line equation (Eq. (11)) is obtained from two successive decouplings (see the Appendix of [22]), as depicted in Fig. 2.

Note that in Eq. (11), the matrix product $(\mathbf{Y}_{\text{gm}})^{+}\mathbf{Y}_{\text{gg}}$ condenses the dynamics of the global set of DoFs g to the set of DoFs m. In particular, the FRFs $\mathbf{Y}_{\text{gm}}$ relates the response $\boldsymbol{u}_{\text{g}}$ at the global set of DoFs g of the parent model, to a set of forces $\tilde{\boldsymbol{g}}_{\text{m}}$ applied to the set of DoFs m:

$$\tilde{\boldsymbol{g}}_{\text{m}} = (\mathbf{Y}_{\text{gm}})^{+}\boldsymbol{u}_{\text{g}} \tag{12}$$

The matrix product $\mathbf{Y}_{\text{gg}}(\mathbf{Y}_{\text{mg}})^{+}$ expands the dynamics of the set of DoFs m to the global set of DoFs g. In particular, the FRF $\mathbf{Y}_{\text{mg}}$ relates the response $\boldsymbol{u}_{\text{m}}$ at the set of DoFs m, with the forces $\tilde{\boldsymbol{g}}_{\text{g}}$ at the global set of DoFs g:

$$\tilde{\boldsymbol{g}}_{\text{g}} = (\mathbf{Y}_{\text{mg}})^{+}\boldsymbol{u}_{\text{m}} \tag{13}$$

The two matrix products applied to the FRFs $\mathbf{Y}^{\text{par}}_{\text{mm}}$ of the parent model at DoFs m give the removed model, while when they are applied to the overlay model $\mathbf{Y}_{\text{ov}}$, add the measured dynamics to the parent model. Eq. (11) can be written in a different form as:

$$\mathbf{Y}^{\text{hyb}} = \begin{bmatrix} \mathbf{Y}^{\text{par}}_{\text{mm}} & \mathbf{Y}^{\text{par}}_{\text{mv}} & \mathbf{Y}^{\text{par}}_{\text{mc}} \\ \mathbf{Y}^{\text{par}}_{\text{vm}} & \mathbf{Y}^{\text{par}}_{\text{vv}} & \mathbf{Y}^{\text{par}}_{\text{vc}} \\ \mathbf{Y}^{\text{par}}_{\text{cm}} & \mathbf{Y}^{\text{par}}_{\text{cv}} & \mathbf{Y}^{\text{par}}_{\text{cc}} \end{bmatrix} - \begin{bmatrix} \mathbf{Y}^{\text{par}}_{\text{mg}}(\mathbf{Y}^{\text{par}}_{\text{mg}})^{+} \\ \mathbf{Y}^{\text{par}}_{\text{vg}}(\mathbf{Y}^{\text{par}}_{\text{mg}})^{+} \\ \mathbf{Y}^{\text{par}}_{\text{cg}}(\mathbf{Y}^{\text{par}}_{\text{mg}})^{+} \end{bmatrix} (\mathbf{Y}^{\text{par}}_{\text{mm}} - \mathbf{Y}^{\text{ov}}_{\text{mm}}) \begin{bmatrix} (\mathbf{Y}^{\text{par}}_{\text{gm}})^{+}\mathbf{Y}^{\text{par}}_{\text{gm}} & (\mathbf{Y}^{\text{par}}_{\text{gm}})^{+}\mathbf{Y}^{\text{par}}_{\text{gv}} & (\mathbf{Y}^{\text{par}}_{\text{gm}})^{+}\mathbf{Y}^{\text{par}}_{\text{gc}} \end{bmatrix} \tag{14}$$

[1] The Extended SEMM is chosen for this study instead of the Standard/Basic SEMM, as the latter can cause the appearance of spurious peaks in the expanded model.

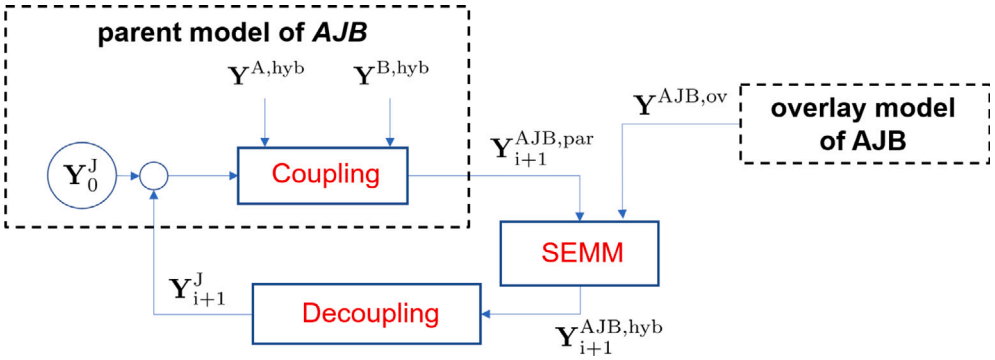

Fig. 3. Workflow of the iterative identification procedure.

For the properties of the left and right pseudo-inverses, one has:

$$\mathbf{Y}^{par}_{mg}(\mathbf{Y}^{par}_{mg})^{+} = \mathbf{I}_{mm}; \quad (\mathbf{Y}^{par}_{gm})^{+}\mathbf{Y}^{par}_{gm} = \mathbf{I}_{mm} \tag{15}$$

It is clear from Eq. (14) that in correspondence with the measured DoFs m, SEMM simply replaces the dynamics of the parent model with the measured dynamics of the overlay model, i.e.:

$$\mathbf{Y}^{hyb}_{mm} = \mathbf{Y}^{ov}_{mm} \tag{16}$$

Instead, at the other DoFs, the overlay dynamics are expanded on the numerical ones.

2.3. Joint identification procedure

The joint identification procedure, summarized in Fig. 3, is developed considering that the coupling DoFs are not accessible for measurements. To perform decoupling, FRFs of the assembled system AJB at the coupling DoFs c are necessary; thus, SEMM expansion technique can be used. In this way, the dynamic behavior of the joint J is identified through the decoupling procedure, using the hybrid model of the whole system AJB containing the coupling DoFs c and the hybrid models of subsystems A and B. However, to obtain the hybrid model of the whole system AJB, a parent model is needed. This can be obtained by coupling the hybrid models of the subsystems A and B with an initial guess model of the joint J, as described in Appendix. Since the real model of the joint J is unknown, the joint identification procedure is iterative. At the first iteration, a guess model $\mathbf{Y}^{J}_{0}$ of the joint must be provided. By performing a SEMM expansion on the parent model $\mathbf{Y}^{AJB,par}_{i+1}$, using the experimental overlay model $\mathbf{Y}^{AJB,ov}$, the hybrid model $\mathbf{Y}^{AJB,hyb}_{i+1}$ is obtained. At this point, the decoupling can be performed to find a model for the joint $\mathbf{Y}^{J}_{i+1}$. This model is used in Eq. (56) at the following iterative step to reach convergence. The iterative algorithm stops when the following convergence criterion is satisfied:

$$\frac{\left|(\mathbf{Y}^{AJB,par}_{mm})_{i+1} - \mathbf{Y}^{AJB,ov}\right|_2}{\left|\mathbf{Y}^{AJB,ov}\right|_2} < \varepsilon \tag{17}$$

i.e., when the parent model at iteration i+1 and the overlay model are very close on the set of measurement DoFs m. By looking at Eq. (11), this means that the SEMM expansion cannot further update the parent model. The FRFs matrix of the identified joint $\mathbf{Y}^{J}$ shows the dynamic behavior of the joint and, in particular, its natural frequencies. Also, by inverting this matrix, it is possible to obtain the corresponding dynamic stiffness matrix $\mathbf{Z}^{J}$ useful to identify the physical properties of the joint.

In [25], it was noted that when using an extended interface, the procedure does not converge even in a large number of iterations, because the measured dynamics are expanded equally on all the DoFs. To achieve convergence in a smaller number of iterations, the authors of [25] proposed to use weighted pseudo-inversion to perform matrix inversions in the SEMM expansion of the assembled system. In this process, the coupling DoFs c are given a significantly larger weight than the others. A more mathematical discussion of the role of weights is given in Section 5.1. However, the results obtained are highly affected by spurious peaks, as the weights assigned in this way affect the conditioning of the SEMM matrices to be inverted and consequently that of the IFM. In this paper, the use of a pseudo-interface in the decoupling step, rather than an extended interface, is proposed to improve the solution. Moreover, a discussion is made about using the extended interface, and strategies to improve its solution are suggested.

3. Sources of error in the identification procedure

The described identification procedure can be ill-conditioned, i.e., small errors in the data can be largely amplified in the solution. The sources of error propagation can be found in matrix inversions. In this procedure, two main steps can be a source of error propagation: the decoupling and the SEMM expansion on the assembled system RU.

3.1. Interface flexibility matrix inversion

As remarked in Section 2.3, the FRF matrix of the unknown joint J is identified by decoupling the hybrid model of the residual subsystem R from the hybrid model of the assembled system RU.[2] In Eq. (7), the inversion of the IFM plays a crucial role in the obtained solution. The conditioning of the IFM depends on the choice of the decoupling interface. Here, the expression of the IFM for two types of interfaces (the extended and the pseudo-interface) are obtained and compared, highlighting the differences in terms of error propagation. With the partitioning of DoFs into measurement m, validation v and coupling c DoFs introduced in Section 2.2, the response vector $\boldsymbol{u}$ and the uncoupled FRF matrix $\mathbf{Y}$ in Eq. (2), have the following expression:

$$\boldsymbol{u} = \begin{Bmatrix} \boldsymbol{u}_{\mathrm{m}}^{\mathrm{RU}} \\ \boldsymbol{u}_{\mathrm{v}}^{\mathrm{RU}} \\ \boldsymbol{u}_{\mathrm{c}}^{\mathrm{RU}} \\ \boldsymbol{u}_{\mathrm{m}}^{\mathrm{R}} \\ \boldsymbol{u}_{\mathrm{v}}^{\mathrm{R}} \\ \boldsymbol{u}_{\mathrm{c}}^{\mathrm{R}} \end{Bmatrix}, \quad \mathbf{Y} = \begin{bmatrix} \mathbf{Y}_{\mathrm{mm}}^{\mathrm{RU,hyb}} & \mathbf{Y}_{\mathrm{mv}}^{\mathrm{RU,hyb}} & \mathbf{Y}_{\mathrm{mc}}^{\mathrm{RU,hyb}} & & & \\ \mathbf{Y}_{\mathrm{vm}}^{\mathrm{RU,hyb}} & \mathbf{Y}_{\mathrm{vv}}^{\mathrm{RU,hyb}} & \mathbf{Y}_{\mathrm{vc}}^{\mathrm{RU,hyb}} & & & \\ \mathbf{Y}_{\mathrm{cm}}^{\mathrm{RU,hyb}} & \mathbf{Y}_{\mathrm{cv}}^{\mathrm{RU,hyb}} & \mathbf{Y}_{\mathrm{cc}}^{\mathrm{RU,hyb}} & & & \\ & & & -\mathbf{Y}_{\mathrm{mm}}^{\mathrm{R,hyb}} & -\mathbf{Y}_{\mathrm{mv}}^{\mathrm{R,hyb}} & -\mathbf{Y}_{\mathrm{mc}}^{\mathrm{R,hyb}} \\ & & & -\mathbf{Y}_{\mathrm{vm}}^{\mathrm{R,hyb}} & -\mathbf{Y}_{\mathrm{vv}}^{\mathrm{R,hyb}} & -\mathbf{Y}_{\mathrm{vc}}^{\mathrm{R,hyb}} \\ & & & -\mathbf{Y}_{\mathrm{cm}}^{\mathrm{R,hyb}} & -\mathbf{Y}_{\mathrm{cv}}^{\mathrm{R,hyb}} & -\mathbf{Y}_{\mathrm{cc}}^{\mathrm{R,hyb}} \end{bmatrix} \tag{18}$$

The boolean matrix $\mathbf{B}$ can be written as:

$$\boldsymbol{B} = \left[\mathbf{B}^{\mathrm{RU}} \;\middle|\; \mathbf{B}^{\mathrm{R}}\right] \tag{19}$$

Using Eq. (19), the IFM can be written as:

$$\mathbf{B}\mathbf{Y}\mathbf{B}^{T} = \mathbf{B}^{\mathrm{RU}}\mathbf{Y}^{\mathrm{RU,hyb}}\mathbf{B}^{\mathrm{RU}T} - \mathbf{B}^{\mathrm{R}}\mathbf{Y}^{\mathrm{R,hyb}}\mathbf{B}^{\mathrm{R}T} \tag{20}$$

The boolean matrix $\mathbf{B}$ and the IFM matrix defined in Eq. (20) can be specified for the particular type of interface.

3.1.1. Extended interface

In the extended interface, the coupling DoFs c and a subset of the internal DoFs ($i \subseteq r$) of subsystems R are considered. In particular, when the internal DoFs i are the measured DoFs m, the compatibility conditions are:

$$\begin{cases} \boldsymbol{u}_{\mathrm{c}}^{\mathrm{RU}} - \boldsymbol{u}_{\mathrm{c}}^{\mathrm{R}} = 0 \\ \boldsymbol{u}_{\mathrm{m}}^{\mathrm{RU}} - \boldsymbol{u}_{\mathrm{m}}^{\mathrm{R}} = 0 \end{cases} \tag{21}$$

These conditions can be written using the signed boolean matrix $\mathbf{B}$:

$$\mathbf{B} = \left[\begin{array}{ccc|ccc} \mathbf{0} & \mathbf{0} & \mathbf{I} & \mathbf{0} & \mathbf{0} & -\mathbf{I} \\ \mathbf{I} & \mathbf{0} & \mathbf{0} & -\mathbf{I} & \mathbf{0} & \mathbf{0} \end{array}\right] \tag{22}$$

According to Eq. (20), the IFM matrix can be written as follows:

$$\mathbf{B}\mathbf{Y}\mathbf{B}^{T} = \begin{bmatrix} \mathbf{Y}_{\mathrm{cc}}^{\mathrm{RU,hyb}} & \mathbf{Y}_{\mathrm{cm}}^{\mathrm{RU,hyb}} \\ \mathbf{Y}_{\mathrm{mc}}^{\mathrm{RU,hyb}} & \mathbf{Y}_{\mathrm{mm}}^{\mathrm{RU,hyb}} \end{bmatrix} - \begin{bmatrix} \mathbf{Y}_{\mathrm{cc}}^{\mathrm{R,hyb}} & \mathbf{Y}_{\mathrm{cm}}^{\mathrm{R,hyb}} \\ \mathbf{Y}_{\mathrm{mc}}^{\mathrm{R,hyb}} & \mathbf{Y}_{\mathrm{mm}}^{\mathrm{R,hyb}} \end{bmatrix} \tag{23}$$

Information of the hybrid models of both R and RU at the coupling DoFs c and at the measured DoFs m appear in the expression of the IFM. The term in Eq. (23) related to the hybrid model of the assembled system RU, can be written using Eqs. (14) and (56):

$$\begin{aligned} \mathbf{B}\mathbf{Y}\mathbf{B}^{T} = {} & \begin{bmatrix} \mathbf{Y}_{\mathrm{cc}}^{\mathrm{R,hyb}} & \mathbf{Y}_{\mathrm{cm}}^{\mathrm{R,hyb}} \\ \mathbf{Y}_{\mathrm{mc}}^{\mathrm{R,hyb}} & \mathbf{Y}_{\mathrm{cc}}^{\mathrm{R,hyb}} \end{bmatrix} - \begin{bmatrix} \mathbf{Y}_{\mathrm{cc}}^{\mathrm{R,hyb}} \\ \mathbf{Y}_{\mathrm{mc}}^{\mathrm{R,hyb}} \end{bmatrix} (\mathbf{Y}_{\mathrm{cc}}^{\mathrm{R,hyb}} + \mathbf{Y}_{\mathrm{cc}}^{\mathrm{J}})^{-1} \begin{bmatrix} \mathbf{Y}_{\mathrm{cc}}^{\mathrm{R,hyb}} & \mathbf{Y}_{\mathrm{cm}}^{\mathrm{R,hyb}} \end{bmatrix} \\ & + \begin{bmatrix} \mathbf{Y}_{\mathrm{cg}}^{\mathrm{RU,par}} (\mathbf{Y}_{\mathrm{mg}}^{\mathrm{RU,par}})^{+} \\ \mathbf{Y}_{\mathrm{mg}}^{\mathrm{RU,par}} (\mathbf{Y}_{\mathrm{mg}}^{\mathrm{RU,par}})^{+} \end{bmatrix} (\mathbf{Y}_{\mathrm{mm}}^{\mathrm{RU,ov}} - \mathbf{Y}_{\mathrm{mm}}^{\mathrm{RU,par}}) \begin{bmatrix} (\mathbf{Y}_{\mathrm{gm}}^{\mathrm{RU,par}})^{+} \mathbf{Y}_{\mathrm{gc}}^{\mathrm{RU,par}} & (\mathbf{Y}_{\mathrm{gm}}^{\mathrm{RU,par}})^{+} \mathbf{Y}_{\mathrm{gm}}^{\mathrm{RU,par}} \end{bmatrix} - \begin{bmatrix} \mathbf{Y}_{\mathrm{cc}}^{\mathrm{R,hyb}} & \mathbf{Y}_{\mathrm{cm}}^{\mathrm{R,hyb}} \\ \mathbf{Y}_{\mathrm{mc}}^{\mathrm{R,hyb}} & \mathbf{Y}_{\mathrm{cc}}^{\mathrm{R,hyb}} \end{bmatrix} \end{aligned} \tag{24}$$

Note that in Eq. (24), the contribution of the hybrid model of the residual substructure R cancels out. Moreover, the term $\mathbf{Y}_{\mathrm{mm}}^{\mathrm{RU,par}}$ can be substituted using part of Eq. (56):

$$\mathbf{Y}_{\mathrm{mm}}^{\mathrm{RU,par}} = \mathbf{Y}_{\mathrm{mm}}^{\mathrm{R,hyb}} - \mathbf{Y}_{\mathrm{mc}}^{\mathrm{R,hyb}} (\mathbf{Y}_{\mathrm{cc}}^{\mathrm{R,hyb}} + \mathbf{Y}_{\mathrm{cc}}^{\mathrm{J}})^{-1} \mathbf{Y}_{\mathrm{cm}}^{\mathrm{R,hyb}} \tag{25}$$

[2] Although in joint identification through decoupling both symbols U and J denote the unknown joint subsystem, in the rest of the paper U is used only when the joint is within the assembled system RU such that the decoupling notation introduced in Section 2.1 is followed. Instead, J is used when the joint is intended as a standalone subsystem.

obtaining:

$$\begin{aligned}\mathbf{BYB}^T = &-\begin{bmatrix}\mathbf{Y}_{cc}^{R,hyb}\\ \mathbf{Y}_{mc}^{R,hyb}\end{bmatrix}\left(\mathbf{Y}_{cc}^{R,hyb}+\mathbf{Y}_{cc}^{J}\right)^{-1}\begin{bmatrix}\mathbf{Y}_{cc}^{R,hyb} & \mathbf{Y}_{cm}^{R,hyb}\end{bmatrix}\\ &+\begin{bmatrix}\mathbf{Y}_{cg}^{RU,par}(\mathbf{Y}_{mg}^{RU,par})^{+}\\ \mathbf{Y}_{mg}^{RU,par}(\mathbf{Y}_{mg}^{RU,par})^{+}\end{bmatrix}\left(\mathbf{Y}_{mm}^{RU,ov}-\mathbf{Y}_{mm}^{R,hyb}\right)\begin{bmatrix}(\mathbf{Y}_{gm}^{RU,par})^{+}\mathbf{Y}_{gc}^{RU,par} & (\mathbf{Y}_{gm}^{RU,par})^{+}\mathbf{Y}_{gm}^{RU,par}\end{bmatrix}\\ &+\begin{bmatrix}\mathbf{Y}_{cg}^{RU,par}(\mathbf{Y}_{mg}^{RU,par})^{+}\\ \mathbf{Y}_{mg}^{RU,par}(\mathbf{Y}_{mg}^{RU,par})^{+}\end{bmatrix}\mathbf{Y}_{mc}^{R,hyb}\left(\mathbf{Y}_{cc}^{R,hyb}+\mathbf{Y}_{cc}^{J}\right)^{-1}\mathbf{Y}_{cm}^{R,hyb}\begin{bmatrix}(\mathbf{Y}_{gm}^{RU,par})^{+}\mathbf{Y}_{gc}^{RU,par} & (\mathbf{Y}_{gm}^{RU,par})^{+}\mathbf{Y}_{gm}^{RU,par}\end{bmatrix}\end{aligned} \tag{26}$$

In this case, the IFM can be split into three matrices. The second one depends on the difference $(\mathbf{Y}_{mm}^{RU,ov}-\mathbf{Y}_{mm}^{R,ov})$ between the measured dynamics of the assembled system *RU* and of the residual substructure *R*. Since these dynamics come from experimental measurements, they can be affected by noise and measurement errors. Instead, the dynamics of the first and third terms of Eq. (26) come from an expansion process. Thus, they are also affected by expansion errors. As a consequence, both measurement errors and expansion errors can propagate in the solution because of the inversion of the IFM matrix.

3.1.2. Pseudo interface

The use of a pseudo-interface (defined in Section 2.1) is proposed in this paper to improve the results of the identification procedure. In the pseudo-interface, only internal DoFs ($i \subseteq r$) of subsystem *R* are considered. Here, in particular, compatibility and equilibrium are imposed on the measured DoFs *m*. The compatibility conditions become:

$$\boldsymbol{u}_m^{RU}-\boldsymbol{u}_m^{R}=0 \tag{27}$$

Eq. (27) can be written in the compact form of Eq. (3) using the boolean matrix **B**:

$$\mathbf{B}=\left[\mathbf{I}\quad\mathbf{0}\quad\mathbf{0}\;\middle|\;-\mathbf{I}\quad\mathbf{0}\quad\mathbf{0}\right] \tag{28}$$

The corresponding expression of the IFM matrix is:

$$\mathbf{BYB}^T=\mathbf{Y}_{mm}^{RU,hyb}-\mathbf{Y}_{mm}^{R,hyb}=\mathbf{Y}_{mm}^{RU,ov}-\mathbf{Y}_{mm}^{R,ov} \tag{29}$$

When a pseudo-interface is used, only the measured dynamics $\mathbf{Y}_{mm}^{RU,ov}$ of the assembled structure *RU* and $\mathbf{Y}_{mm}^{R,ov}$ of the residual subsystem *R* appear in the expression of the IFM matrix. These dynamics can be affected by measurement errors and noise, but they do not contain any expansion error.

3.2. SEMM interface matrices inversion

The second source of error in the procedure can be found in the inversion of the two non-square matrices $\mathbf{Y}_{mg}^{AJB,par}$ and $\mathbf{Y}_{gm}^{AJB,par}$ in the SEMM expansion performed on the assembled system *AJB* (see Eq. (11)). In principle, these two matrices belong to a parent numerical model and should not be affected by noise. However, in the present iterative procedure, the parent model is generated by coupling the hybrid models of the subsystems *A* and *B* and the joint model identified at the previous iteration. The hybrid models of the subsystems *A* and *B* are affected by measurement noise and expansion error, while the identified joint model can be affected by the ill-conditioning of the IFM as discussed in Section 3.1. For this reason, particular care must be taken when computing the pseudo-inverse of the two matrices $\mathbf{Y}_{mg}^{AJB,par}$ and $\mathbf{Y}_{gm}^{AJB,par}$.

4. Improving the conditioning of the identification procedure

In this Section, two ways are proposed to improve the solution of the procedure. The first one (Section 4.1) aims at filtering out the spurious peaks that are present in the identified joint FRFs. The second one (Section 4.2) aims to reduce the procedure's error propagation by selecting an advantageous decoupling interface.

4.1. Estimation of the mass, damping, and stiffness matrices of the identified joint

When spurious peaks are present in the identified joint FRF matrix, the corresponding dynamic stiffness matrix $\mathbf{Z}^J$, obtained through the inversion of the FRF matrix $\mathbf{Y}^J$ is also affected by error propagation, but it maintains important physical information. Therefore, at the end of the iterative procedure, it can be convenient to fit the real and the imaginary part of every single term Z_{hk}^J of the identified dynamic stiffness matrix with three parameters m_{hk}^J, c_{hk}^J and k_{hk}^J that represent, respectively, the mass, damping, and stiffness coefficients associated to the pair of DoFs *h* and *k*. A least squares fitting is performed on a proper frequency band where the identified dynamic stiffness shows a smooth and regular behavior, thus minimizing the possible influence of measurement errors or spurious peaks on the accuracy of the process. The estimated matrices of mass $\mathbf{M}^{J,est}$, damping $\mathbf{C}^{J,est}$ and stiffness $\mathbf{K}^{J,est}$ can be used to express the dynamic stiffness matrix $\mathbf{Z}^{J,est}$ in the whole frequency range considered:

$$\mathbf{Z}^{J,est}=-\omega^2\mathbf{M}^{J,est}+j\omega\mathbf{C}^{J,est}+\mathbf{K}^{J,est} \tag{30}$$

and through its inversion, the accelerance FRF matrix $\mathbf{Y}^{\mathrm{J,est}}$ of the joint model:

$$\mathbf{Y}^{\mathrm{J,est}} = -\omega^2 (\mathbf{Z}^{\mathrm{J,est}})^{-1} \tag{31}$$

The FRF matrix in Eq. (31) represents a filtered solution for the joint model and can be used to predict the dynamic behavior of the assembled system $\mathbf{Y}^{\mathrm{AJB,est}}$. In this way, it is possible to obtain a better estimation of the FRFs and the physical properties of the joint.

4.2. Selection of the decoupling interface to improve conditioning and fasten convergence

In Section 3.1, the expressions of the IFM matrix using an extended or a pseudo-interface within the iterative identification procedure are presented. Firstly, as it is shown in the following Section 7.2, the conditioning of the IFM improves if a pseudo-interface is used in the decoupling rather than an extended interface. This implies less error propagation in the inversion of the IFM, with the benefit of getting a better solution. Secondly, the pseudo-interface is defined only on the measured DoFs m (Eq. (29)), and consequently, the propagation of the expansion error due to the coupling DoFs c is avoided. Finally, to reach convergence when using an extended interface, a weighting process in the SEMM expansion procedure of the assembled system is needed. In particular, a much higher weight should be assigned to the coupling DoFs c rather than to the other DoFs. However, this weighting worsens the conditioning of the procedure, giving a solution strongly affected by error propagation. Strategies to improve this solution are proposed in the following Section.

5. Improving the solution with the extended interface through TSVD

Here, the weighting procedure in the SEMM equation proposed in [25] and described in Section 2.3, is introduced. The equations for the weighted pseudo inverses are discussed, together with the consequences in terms of force identifications (Section 5.1). Furthermore, the effects on the procedure of the weights introduced in the SEMM expansion of the assembled system when using the extended interface are analyzed. Particular attention is given to the conditioning of the SEMM matrices and on the IFM matrix. Two different strategies are proposed to improve this solution. Both strategies are based on the use of the Truncated Singular Value Decomposition (TSVD), because the introduced weights clearly indicate the number of singular values to be retained (this is true under the assumption that observability and controllability are sufficient, i.e. that all significant singular values are related to relevant dynamic behavior). In the first strategy (strategy A in Section 5.1.1), the TSVD is applied only on the IFM, while in the second one (strategy B in Section 5.1.2), the TSVD is applied in both the SEMM interface matrices and in the IFM.

5.1. Weighted extended-SEMM expansion

When performing SEMM, it is possible to focus the expansion on a subset of DoFs. This is done by computing the two pseudo-inverses $(\mathbf{Y}^{\mathrm{par}}_{\mathrm{mg}})^{+}$ and $(\mathbf{Y}^{\mathrm{par}}_{\mathrm{gm}})^{+}$ through weighted pseudo-inverses [27] (the superscripts $^{\mathrm{AJB}}$ and $^{\mathrm{par}}$ are omitted for clarity):

$$(\mathbf{Y}_{\mathrm{mg}})^{W,+} = \mathbf{W}\mathbf{Y}^{H}_{\mathrm{mg}}(\mathbf{Y}_{\mathrm{mg}}\mathbf{W}\mathbf{Y}^{H}_{\mathrm{mg}})^{-1} = \mathbf{M}(\mathbf{Y}_{\mathrm{mg}}\mathbf{M})^{+} \tag{32}$$

$$(\mathbf{Y}_{\mathrm{gm}})^{W,+} = (\mathbf{Y}^{H}_{\mathrm{gm}}\mathbf{W}\mathbf{Y}_{\mathrm{gm}})^{-1}\mathbf{Y}^{H}_{\mathrm{gm}}\mathbf{W} = (\mathbf{M}\mathbf{Y}_{\mathrm{gm}})^{+}\mathbf{M} \tag{33}$$

where $\mathbf{W} = \mathbf{M}^{H}\mathbf{M}$ is a weighting matrix that assign a different weight to the different sets of DoFs:

$$\mathbf{W} = \begin{bmatrix} w_{\mathrm{m}}\mathbf{I}_{\mathrm{mm}} & & \\ & w_{\mathrm{v}}\mathbf{I}_{\mathrm{vv}} & \\ & & w_{\mathrm{c}}\mathbf{I}_{\mathrm{cc}} \end{bmatrix}; \qquad \mathbf{M} = \begin{bmatrix} \sqrt{w_{\mathrm{m}}}\mathbf{I}_{\mathrm{mm}} & & \\ & \sqrt{w_{\mathrm{v}}}\mathbf{I}_{\mathrm{vv}} & \\ & & \sqrt{w_{\mathrm{c}}}\mathbf{I}_{\mathrm{cc}} \end{bmatrix} \tag{34}$$

A physical interpretation of the weighting is given in the following for the two pseudo-inverses.

The right weighted pseudo-inverse defined in Eq. (33) solves the problem in Eq. (12) for the interface forces $\tilde{\boldsymbol{g}}_{\mathrm{m}}$ in a least-square sense by minimizing the error $\|\boldsymbol{\mu}_{\mathrm{g}}\|^2_{\mathrm{M}} = \boldsymbol{\mu}_{\mathrm{g}}{}^{H}\mathbf{W}\boldsymbol{\mu}_{\mathrm{g}}$, with $\boldsymbol{\mu}_{\mathrm{g}} = \boldsymbol{u}_{\mathrm{g}} - \mathbf{Y}_{\mathrm{gm}}\tilde{\boldsymbol{g}}_{\mathrm{m}}$:

$$\begin{aligned} \|\boldsymbol{\mu}_{\mathrm{g}}\|^2_{\mathrm{M}} &= (\boldsymbol{u}_{\mathrm{m}} - \mathbf{Y}_{\mathrm{mm}}\tilde{\boldsymbol{g}}_{\mathrm{m}})^{H} w_{\mathrm{m}} (\boldsymbol{u}_{\mathrm{m}} - \mathbf{Y}_{\mathrm{mm}}\tilde{\boldsymbol{g}}_{\mathrm{m}}) + (\boldsymbol{u}_{\mathrm{v}} - \mathbf{Y}_{\mathrm{vm}}\tilde{\boldsymbol{g}}_{\mathrm{m}})^{H} w_{\mathrm{v}} (\boldsymbol{u}_{\mathrm{v}} - \mathbf{Y}_{\mathrm{vm}}\tilde{\boldsymbol{g}}_{\mathrm{m}}) \\ &+ (\boldsymbol{u}_{\mathrm{c}} - \mathbf{Y}_{\mathrm{cm}}\tilde{\boldsymbol{g}}_{\mathrm{m}})^{H} w_{\mathrm{c}} (\boldsymbol{u}_{\mathrm{c}} - \mathbf{Y}_{\mathrm{cm}}\tilde{\boldsymbol{g}}_{\mathrm{m}}) \end{aligned} \tag{35}$$

When a higher weight is assigned to a particular set of DoFs, the pseudo-forces $\tilde{\boldsymbol{g}}_{\mathrm{m}}$ mostly minimize the error on the response of that set of DoFs. The expression of the pseudo-forces $\tilde{\boldsymbol{g}}_{\mathrm{m}}$ can be obtained by rewriting Eq. (33) as:

$$(\mathbf{Y}_{\mathrm{gm}})^{W,+} = \hat{\boldsymbol{\Delta}}^{-1}_{\mathrm{mm}}\mathbf{Y}^{H}_{\mathrm{gm}}\mathbf{W} = \begin{bmatrix} w_{\mathrm{m}}\hat{\boldsymbol{\Delta}}^{-1}_{\mathrm{mm}}\mathbf{Y}^{H}_{\mathrm{mm}} & w_{\mathrm{v}}\hat{\boldsymbol{\Delta}}^{-1}_{\mathrm{mm}}\mathbf{Y}^{H}_{\mathrm{vm}} & w_{\mathrm{c}}\hat{\boldsymbol{\Delta}}^{-1}_{\mathrm{mm}}\mathbf{Y}^{H}_{\mathrm{cm}} \end{bmatrix} \tag{36}$$

where

$$\hat{\boldsymbol{\Delta}}_{\mathrm{mm}} = \mathbf{Y}^{H}_{\mathrm{gm}}\mathbf{W}\mathbf{Y}_{\mathrm{gm}} = w_{\mathrm{m}}\mathbf{Y}^{H}_{\mathrm{mm}}\mathbf{Y}_{\mathrm{mm}} + w_{\mathrm{v}}\mathbf{Y}^{H}_{\mathrm{vm}}\mathbf{Y}_{\mathrm{vm}} + w_{\mathrm{c}}\mathbf{Y}^{H}_{\mathrm{cm}}\mathbf{Y}_{\mathrm{cm}} \tag{37}$$

By substituting Eq. (36) into Eq. (12) one has:

$$\boldsymbol{g}_{\mathrm{m}} = w_{\mathrm{m}}\hat{\boldsymbol{\Delta}}^{-1}_{\mathrm{mm}}\mathbf{Y}^{H}_{\mathrm{mm}}\boldsymbol{u}_{\mathrm{m}} + w_{\mathrm{v}}\hat{\boldsymbol{\Delta}}^{-1}_{\mathrm{mm}}\mathbf{Y}^{H}_{\mathrm{vm}}\boldsymbol{u}_{\mathrm{v}} + w_{\mathrm{c}}\hat{\boldsymbol{\Delta}}^{-1}_{\mathrm{mm}}\mathbf{Y}^{H}_{\mathrm{cm}}\boldsymbol{u}_{\mathrm{c}} \tag{38}$$

When the weight assigned to a particular set of DoFs is much higher than the others, the forces $\boldsymbol{g}_{\mathrm{m}}$ are mainly determined by the responses of the parent model at that set of DoFs.

The left weighted pseudo-inverse defined in Eq. (32) gives the solution for the problem in Eq. (13) for the interface forces $\tilde{\boldsymbol{g}}_{\mathrm{g}}$ that has the minimum norm $\|\tilde{\boldsymbol{g}}_{\mathrm{g}}^{\mathrm{RU,par}}\|_{\mathrm{M}}^2$ and satisfies the constraint $\mathbf{Y}_{\mathrm{mg}}\tilde{\boldsymbol{g}}_{\mathrm{g}} - \boldsymbol{u}_{\mathrm{m}} = \mathbf{0}$. To understand the role of the weights, $(\mathbf{Y}_{\mathrm{mg}})^{W,+}$ can be rewritten as:

$$(\mathbf{Y}_{\mathrm{mg}})^{W,+} = \mathbf{W}\mathbf{Y}_{\mathrm{mg}}^H\tilde{\boldsymbol{\Delta}}_{\mathrm{mm}}^{-1} = \begin{bmatrix} w_{\mathrm{m}}\mathbf{Y}_{\mathrm{mm}}^H\tilde{\boldsymbol{\Delta}}_{\mathrm{mm}}^{-1} \\ w_{\mathrm{v}}\mathbf{Y}_{\mathrm{mv}}^H\tilde{\boldsymbol{\Delta}}_{\mathrm{mm}}^{-1} \\ w_{\mathrm{c}}\mathbf{Y}_{\mathrm{mc}}^H\tilde{\boldsymbol{\Delta}}_{\mathrm{mm}}^{-1} \end{bmatrix} \tag{39}$$

where

$$\tilde{\boldsymbol{\Delta}}_{\mathrm{mm}} = w_{\mathrm{m}}\mathbf{Y}_{\mathrm{mm}}\mathbf{Y}_{\mathrm{mm}}^H + w_{\mathrm{v}}\mathbf{Y}_{\mathrm{mv}}\mathbf{Y}_{\mathrm{mv}}^H + w_{\mathrm{c}}\mathbf{Y}_{\mathrm{mc}}\mathbf{Y}_{\mathrm{mc}}^H \tag{40}$$

Consequently, the forces $\tilde{\boldsymbol{g}}_{\mathrm{g}}$ defined in Eq. (13) are determined as:

$$\tilde{\boldsymbol{g}}_{g} = \begin{bmatrix} w_{\mathrm{m}}\mathbf{Y}_{\mathrm{mm}}^H\tilde{\boldsymbol{\Delta}}_{\mathrm{mm}}^{-1}\boldsymbol{u}_{\mathrm{m}} \\ w_{\mathrm{v}}\mathbf{Y}_{\mathrm{mv}}^H\tilde{\boldsymbol{\Delta}}_{\mathrm{mm}}^{-1}\boldsymbol{u}_{\mathrm{m}} \\ w_{\mathrm{c}}\mathbf{Y}_{\mathrm{mc}}^H\tilde{\boldsymbol{\Delta}}_{\mathrm{mm}}^{-1}\boldsymbol{u}_{\mathrm{m}} \end{bmatrix} \tag{41}$$

When a much higher weight is assigned to a particular set of DoFs, the responses $\boldsymbol{u}_{\mathrm{m}}$ mainly determine the forces applied to that particular set of DoFs. The overall effect is that the expansion is focused on the weighted set of DoFs. However, by assigning the weights in this way, the matrix $\mathbf{M}$ and consequently the matrices $\mathbf{Y}_{\mathrm{mg}}\mathbf{M}$ and $\mathbf{M}\mathbf{Y}_{\mathrm{gm}}$ to be inverted in Eqs. (32) and (33), are ill-conditioned.

5.1.1. Strategy A: TSVD in the IFM

In the first strategy to improve the solution that uses the extended interface, the TSVD is applied on the IFM matrix. In fact, the weights applied on the coupling DoFs c in the SEMM expansion of the assembled system affect the IFM. In particular, it has been noted that in this case, the following relations hold:

$$\begin{cases} \begin{bmatrix} \mathbf{Y}_{\mathrm{cg}}^{\mathrm{RU,par}}(\mathbf{Y}_{\mathrm{mg}}^{\mathrm{RU,par}})^{W,+} \\ \mathbf{Y}_{\mathrm{mg}}^{\mathrm{RU,par}}(\mathbf{Y}_{\mathrm{mg}}^{\mathrm{RU,par}})^{W,+} \end{bmatrix} \mathbf{Y}_{\mathrm{mc}}^{\mathrm{R,hyb}} = \begin{bmatrix} \mathbf{Y}_{\mathrm{cc}}^{\mathrm{R,hyb}} \\ \mathbf{Y}_{\mathrm{mc}}^{\mathrm{R,hyb}} \end{bmatrix} \\ \mathbf{Y}_{\mathrm{cm}}^{\mathrm{R,hyb}} \begin{bmatrix} (\mathbf{Y}_{\mathrm{gm}}^{\mathrm{RU,par}})^{W,+}\mathbf{Y}_{\mathrm{gc}}^{\mathrm{RU,par}} & (\mathbf{Y}_{\mathrm{gm}}^{\mathrm{RU,par}})^{W,+}\mathbf{Y}_{\mathrm{gm}}^{\mathrm{RU,par}} \end{bmatrix} = \begin{bmatrix} \mathbf{Y}_{\mathrm{cc}}^{\mathrm{R,hyb}} & \mathbf{Y}_{\mathrm{cm}}^{\mathrm{R,hyb}} \end{bmatrix} \end{cases} \tag{42}$$

By substituting these two relations in Eq. (26), the first and third term cancels out. It can be easily seen that the rank of the second term is driven by the number N_m of measured DoFs m. As a consequence, the matrix IFM with dimension $(N_c + N_m)\times(N_c + N_m)$ has rank N_m. Consequently, in TSVD, the last N_c singular values are negligible with respect to the first N_m singular values, and thus they have to be discarded. Note that the highest weight is assigned to the N_c coupling DoFs.

5.1.2. Strategy B: TSVD in both SEMM and IFM

In the second strategy to improve the solution, the TSVD is applied in both the SEMM matrices $\mathbf{Y}_{\mathrm{mg}}^{\mathrm{RU,par}}$ and $\mathbf{Y}_{\mathrm{gm}}^{\mathrm{RU,par}}$ and in the IFM matrix. In this case, the effect of the introduced weights is that a number N_c of singular values, associated to $\mathbf{Y}_{\mathrm{cm}}$, become dominant in the SEMM matrices. Retaining only these N_c singular values, when computing the weighted pseudo-inverse, corresponds to considering only the transfer path from the measured DoFs m to the coupling DoFs c [28] to compute the interface forces $\boldsymbol{g}_{\mathrm{m}}$. This is the same as solving the following under-determined problem:

$$\boldsymbol{u}_{\mathrm{c}}^{\mathrm{RU,par}} = \mathbf{Y}_{\mathrm{cm}}^{\mathrm{RU,par}}\tilde{\boldsymbol{g}}_{\mathrm{m}}^{\mathrm{RU,par}} \tag{43}$$

Among the infinite possible solution of Eq. (43), the one that has the minimum norm $\|\tilde{\boldsymbol{g}}_{\mathrm{m}}^{\mathrm{RU,par}}\|_{\mathrm{M}}^2$ and satisfies the constraint $\boldsymbol{u}_{\mathrm{c}}^{\mathrm{RU,par}} - \mathbf{Y}_{\mathrm{cm}}^{\mathrm{RU,par}}\tilde{\boldsymbol{g}}_{\mathrm{m}}^{\mathrm{RU,par}} = \mathbf{0}$ is given by the right Moore–Penrose pseudo inverse:

$$(\mathbf{Y}_{\mathrm{cm}})^{+} = \mathbf{Y}_{\mathrm{cm}}^H(\mathbf{Y}_{\mathrm{cm}}\mathbf{Y}_{\mathrm{cm}}^H)^{-1} \tag{44}$$

Similarly, when weights are assigned to the coupling DoFs c, in the computation of the weighted pseudo-inverse $(\mathbf{Y}_{\mathrm{mg}}^{\mathrm{RU,par}})^{+}$ in Eq. (32), the first N_c singular values are dominant. The truncation of the remaining singular values corresponds to considering only the transfer path from the coupling DoFs c to the measured DoFs m [28] in the estimation of interface forces $\boldsymbol{g}_{\mathrm{c}}$, while the forces on the measured DoFs m and on the validation DoFs v are zero ($\tilde{\boldsymbol{g}}_{\mathrm{m}} = \tilde{\boldsymbol{g}}_{\mathrm{v}} = \mathbf{0}$). This is equivalent to solving the following over-determined problem:

$$\boldsymbol{u}_{\mathrm{m}}^{\mathrm{RU,par}} = \mathbf{Y}_{\mathrm{mc}}^{\mathrm{RU,par}}\tilde{\boldsymbol{g}}_{\mathrm{c}}^{\mathrm{RU,par}} \tag{45}$$

The least-square solution of this problem that minimizes the error $\|\tilde{\boldsymbol{u}}_{\mathrm{m}}^{\mathrm{RU,par}}\|_{\mathrm{M}}^2$ with $\boldsymbol{\mu}_{\mathrm{m}} = \boldsymbol{u}_{\mathrm{m}}^{\mathrm{RU,par}} - \mathbf{Y}_{\mathrm{mc}}^{\mathrm{RU,par}}\tilde{\boldsymbol{g}}_{\mathrm{c}}^{\mathrm{RU,par}}$ is given by the left Moore–Penrose pseudo-inverse:

$$(\mathbf{Y}_{\mathrm{mc}})^{+} = (\mathbf{Y}_{\mathrm{mc}}^H\mathbf{Y}_{\mathrm{mc}})^{-1}\mathbf{Y}_{\mathrm{mc}}^H \tag{46}$$

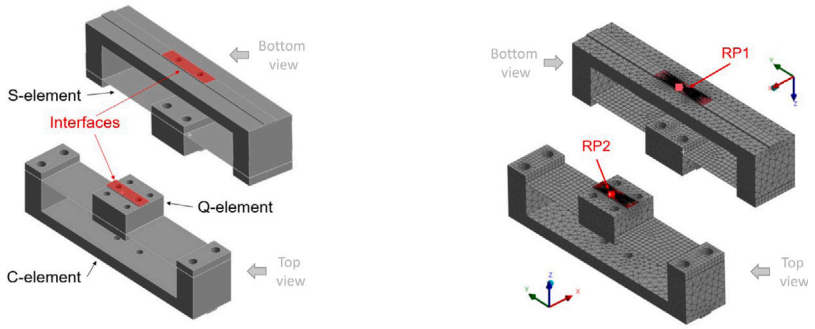

(a) CAD model (b) FE model

Fig. 4. The joint used in the numerical identification is composed of two steel parts (C-element and Q-element) connected together through a 0.2 mm spring steel sheet (S-element). The top and bottom views are both shown for clarity. The dynamic behavior of the joint interfaces is modeled using two remote points.

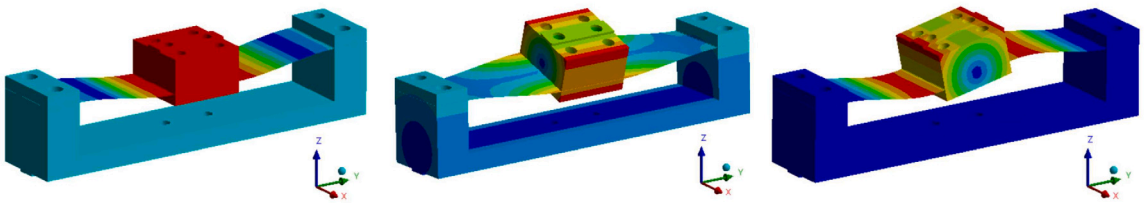

(a) First mode: 6.11 Hz (b) Second mode: 10.7 Hz (c) Third mode: 19.68 Hz

Fig. 5. First three modes of vibration of the joint.

The truncation performed in the SEMM matrices also affects the singular values distribution of the IFM matrix. In this case, each term in Eq. (26), with dimension $(N_c + N_m) \times (N_c + N_m)$ have rank N_c. Consequently, in TSVD, the last N_m singular values are negligible with respect to the first N_c, and thus they must be discarded.

6. Numerical application

The differences in the solution obtained using an extended or a pseudo interface in the decoupling step are first analyzed using numerically generated data. This study is carried out using noise-free data with the aim of demonstrating that, under certain circumstances, the procedure is inherently ill-conditioned and the results are affected by scattering even in the absence of measurement errors. A particular joint that connects two subsystems is used for this investigation. The joint is designed to be tested separately from the other subsystems and to obtain a reference model of the joint useful to validate the identification results.

6.1. Modeling of the joint

The joint considered in this study is the connecting element proposed in [29] and shown in Fig. 4(a), where its top and bottom views are displayed together to highlight the interface surfaces (in red) at which it can be connected to other subsystems. Note that even though the joint can exhibit a nonlinear behavior, in the present work the interest is only on its linear behavior. The joint is composed of two steel parts (C-element and Q-element) connected together through a 0.2 mm spring steel sheet (S-element). The FE model of the joint is developed in ANSYS (Fig. 4(b)), with the only aim of obtaining the reference model needed for validation. The dynamics at the interface surfaces are reduced to that of two remote points RP1 and RP2 located in the middle of the surfaces (as displayed in Fig. 4(b)), using Multi-Point Constraint equations [30,31]. A linear modal analysis is performed to obtain the first 100 modes of vibration of the joint. The FRFs at the remote point DoFs are then generated using the mode superposition method implemented in the pyFBS Python package [32]. This FRFs matrix is the reference model to validate the results. However, only three DoFs are used for each remote point: the translational DoF along the z axis and the two rotational DoFs around the x and y axis. These three DoFs are sufficient to describe the dynamics of the joint, as one can see by looking at the first three modes of vibration of the joint displayed in Fig. 5.

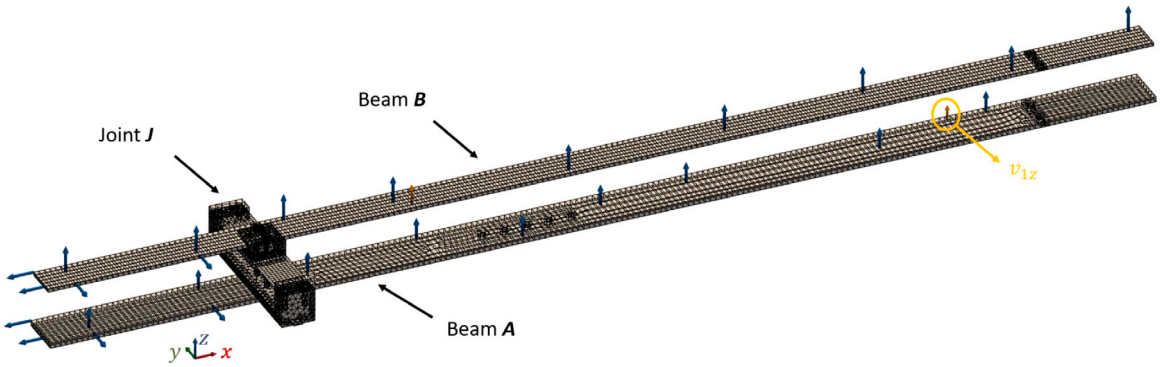

Fig. 6. FE Model of the assembled system. The blue arrows represent the measured DoFs m; the orange arrows represent the validation DoFs v.

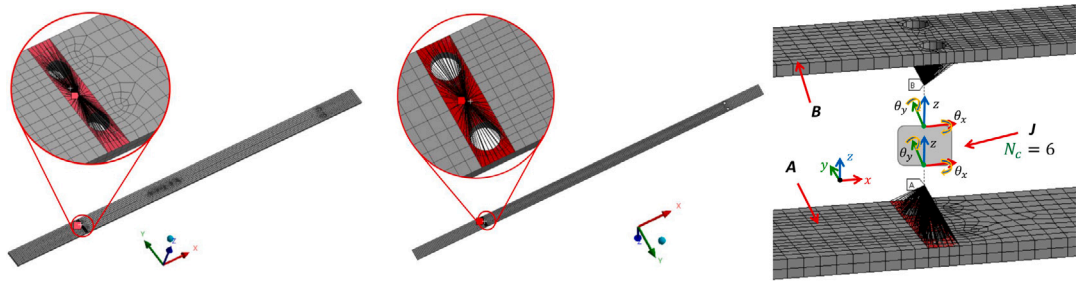

(a) FE model of beam *A* (b) FE model of beam *B* (c) Joint model *J*

Fig. 7. Generation of parent model of the assembled.

6.2. Benchmark structure

The joint described in Fig. 4(a) is used to couple two steel beams A and B that have length of 1 m and cross-section of 40×5 mm and 30×3 mm respectively. The joint element is connected to the beams at a distance of 0.2 m from one of their ends. As seen in 2.3, the parent $\mathbf{Y}_0^{\mathrm{AJB,par}}$ and overlay $\mathbf{Y}^{\mathrm{AJB,ov}}$ models of the assembled structure are needed to perform the identification.

To obtain the overlay model $\mathbf{Y}^{\mathrm{AJB,ov}}$, the FE model of the assembled structure is developed in ANSYS (Fig. 6), and a linear modal analysis is performed to obtain its first 100 modes of vibration of the system. A set of measurement DoFs m (blue arrows) and validation DoFs v (orange arrows) are selected on the structure. For each DoF, both response and excitation are evaluated. The FRFs corresponding to these sets of DoFs are generated using the mode superposition method implemented in pyFBS. In this application, the measured DoF set m for each beam is composed of 2 DoFs in the x direction, 2 DoFs in the y direction, and 9 DoFs in the z direction; globally for the assembled system, a total of 26 measurement DoFs m are required. The validation DoF set v includes 2 DoFs, one on each beam.

As outlined in Fig. 3, to obtain the parent model $\mathbf{Y}_0^{\mathrm{AJB,par}}$ of the assembled structure, first the hybrid models $\mathbf{Y}^{\mathrm{A,hyb}}$ and $\mathbf{Y}^{\mathrm{B,hyb}}$ of the two beams need to be generated. To do so, the two beams are modeled in ANSYS separately, as shown in Figs. 7(a) and 7(b), and linear modal analysis is used to obtain their first 100 modes of vibration. For each beam, the dynamics at the interface surface with the joint are reduced to that of a remote point having three DoFs: the translational DoF along the z axis, and the two rotational DoFs around the x and y axis. The same set of measurement DoFs m and validation DoFs v used for the complete structure are used for the two beams. The set of coupling DoFs c for each beam is composed of the corresponding remote point DoFs. For both beams, the parent model FRFs ($\mathbf{Y}^{\mathrm{A,par}}$ and $\mathbf{Y}^{\mathrm{B,par}}$) and the overlay model FRFs ($\mathbf{Y}^{\mathrm{A,ov}}$ and $\mathbf{Y}^{\mathrm{B,ov}}$) are then obtained using the mode superposition method implemented in pyFBS. Successively, the SEMM expansion is performed to obtain the hybrid model of the separate beams ($\mathbf{Y}^{\mathrm{A,hyb}}$ and $\mathbf{Y}^{\mathrm{B,hyb}}$). Note that since the parent and overlay models of each beam come from the same FE model, in which no noise is added, the hybrid and the parent models coincide. Secondly, the hybrid models of the two beams are coupled to a guess model of the joint, as shown in Fig. 7(c) (the remote points are biased from the surfaces of the beams for displaying purposes). The joint is modeled using 6 DoFs (two translational DoF along the z axis, two rotational DoFs around the x axis, and two rotational DoFs around the y axis), which can be considered as three pairs of uncoupled 2-DoFs systems composed of masses connected through a spring element. The mass and stiffness matrices of the initial guess model of the joint are used to compute the

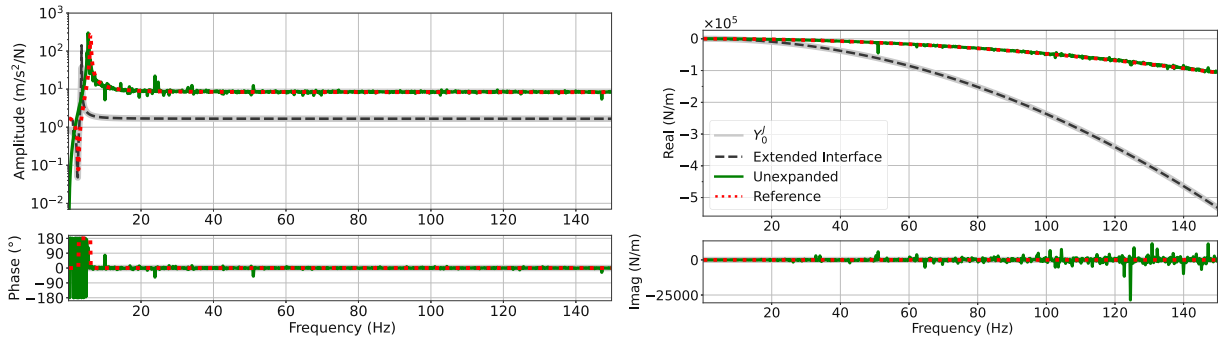

(a) Accelerance FRF (b) Dynamic Stiffness

Fig. 8. Results of the numerical joint identification using an extended interface in the decoupling: (a) drive point FRF $\mathbf{Y}^J$ at DoF q_{2z}; (b) dynamic stiffness $\mathbf{Z}^J$ at DoF q_{2z}.

accelerance FRFs $\mathbf{Y}_0^J$, are:

$$\mathbf{M}_0^J = \begin{bmatrix} m_0 & & & & & \\ & I_{x,0} & & & & \\ & & I_{y,0} & & & \\ & & & m_0 & & \\ & & & & I_{x,0} & \\ & & & & & I_{y,0} \end{bmatrix}; \quad \mathbf{K}_0^J = \begin{bmatrix} K_{z,0}(1+\varepsilon) & & & & -K_{z,0} & \\ & K_{\theta_x,0}(1+\varepsilon) & & & & -K_{\theta_x,0} \\ & & K_{\theta_y,0}(1+\varepsilon) & & & -K_{\theta_y,0} \\ -K_{z,0} & & & K_{z,0} & & \\ & -K_{\theta_x,0} & & & K_{\theta_x,0} & \\ & & -K_{\theta_y,0} & & & K_{\theta_y,0} \end{bmatrix} \tag{47}$$

The parameters used are m_0 =0.6 kg, $I_{x,0} = I_{y,0} = 0.001\,\mathrm{kg\,m^2}$, $K_{z,0}$ =150 N m^{-1}, $K_{\theta_x,0} = K_{\theta_y,0}$ =150 N m rad^{-1}, $\varepsilon = 0.000001$ (ε is a perturbation parameter to avoid singularity). Note that the joint FRF matrix has dimension 6×6.

6.3. Results

This section discusses some results of the numerical joint identification procedure. No perturbations in the data are introduced in this study, as remarked at the beginning of Section 6.

Firstly, it is verified if the SEMM expansion procedure, necessary when the coupling DoFs cannot be measured directly, is affected by error. To this aim, two identifications through substructure decoupling are performed and the results are compared in Fig. 8: in the first one (dashed black line), the SEMM expansion is used to reconstruct the dynamics at the coupling DoFs c starting from numerical FRFs generated at the internal DoFs m; in the second one (solid green line), the FRFs at the coupling DoFs are generated directly by introducing the remote points in the numerical model of the assembled system (see Fig. 6). In both cases an extended decoupling interface is employed (compatibility and equilibrium conditions are imposed on both the measured DoFs m and coupling DoFs c). The reference and initial guess models of the joint are also reported in Fig. 8 by the red and gray lines, respectively. It can be noted that in the second case, where the SEMM expansion is avoided, the joint FRF (Fig. 8(a)) and dynamic stiffness (Fig. 8(b)) associated to the DoF q_{2z}, are correctly identified, even though some scattering effects are present in the results. Instead, when the expansion is employed, the solution coincides with the initial guess model of the joint. In other words, the iterative procedure used in this case does not converge. Comparing the normalized singular values distribution of the IFM in the two cases (Figs. 9(b) and 9(a)), it can be noted that the expansion causes a jump in the distribution in the last N_c singular values. This suggests that the reconstruction of the coupling DoFs c through the expansion does not add independent information in the decoupling step.

To achieve convergence with an extended interface, it is necessary to assign a much higher weight to the coupling DoFs c than to the other DoFs in the SEMM expansion of the assembled system. As a consequence, a clear jump appear the normalized singular values distribution of the IFM (Fig. 9(c)), indicating that the last N_c singular values are insignificant. The FRF and the dynamic stiffness matrices of the joint at DoF q_{2z}, obtained in this case, are shown in Fig. 10 (solid green line). The assigned weights are $w_\mathrm{m} = w_\mathrm{v} = 1\mathrm{e}{-8}$ and $w_\mathrm{c} = 1$. However, the results obtained are strongly affected by scattering. Since no perturbations were added to the numerically simulated FRFs, this shows that the iterative identification procedure is inherently ill-conditioned. This solution can be improved by using strategy A as shown in Fig. 10 by the solid blue line. In this case, only the first $N_m = 18$ singular values are retained when inverting the IFM, which ensures convergence and a correct identification of the joint FRFs while eliminating the scattering in the solution. Similar results are obtained using a pseudo-interface in the decoupling step, as shown by the solid yellow line in Fig. 10. Note that in both cases the joint is correctly identified.

The numerical study also allows analyzing the effect of the choice of the measured DoFs m on the solution, in particular, on the identification of the FRFs at rotational DoFs of the joint. For this purpose, two identifications are performed using two different sets of measured DoFs m, and the solutions are compared in Fig. 11. In the first set, measured DoFs in all directions are used (solution in solid blue line), while in the second one, only measured DoFs in the z direction are used (green solid line). Both solutions in

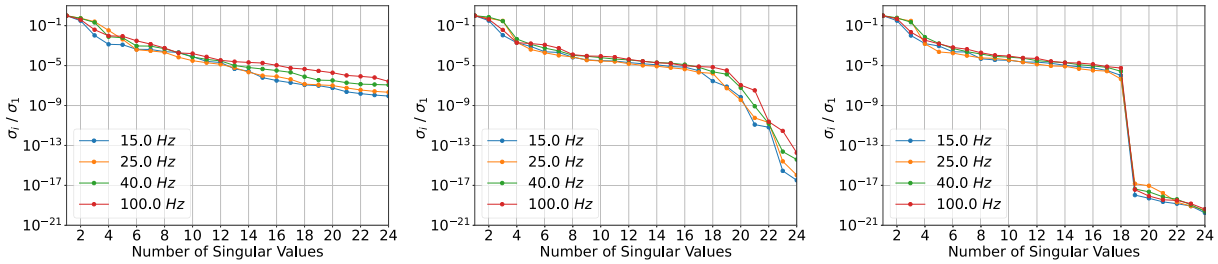

(a) Decoupling without expansion. (b) Iterative procedure without weights in SEMM of AJB. (c) Iterative procedure with weights in SEMM of AJB.

Fig. 9. Normalized singular values distribution σ_i/σ_1 of the IFM using an extended interface in the decoupling step.

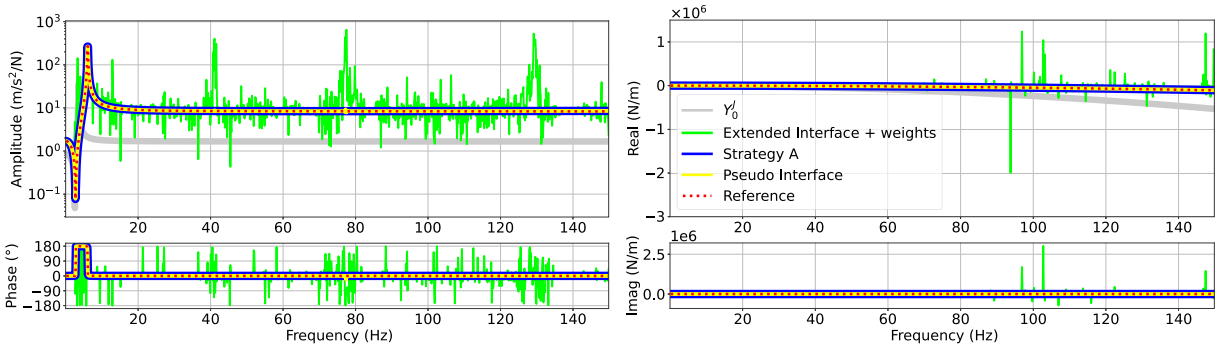

(a) Accelerance FRF (b) Dynamic Stiffness

Fig. 10. Results of the numerical joint identification: (a) drive point FRF $\mathbf{Y}^J$ at DoF q_{2z}; (b) dynamic stiffness $\mathbf{Z}^J$ at DoF q_{2z}.

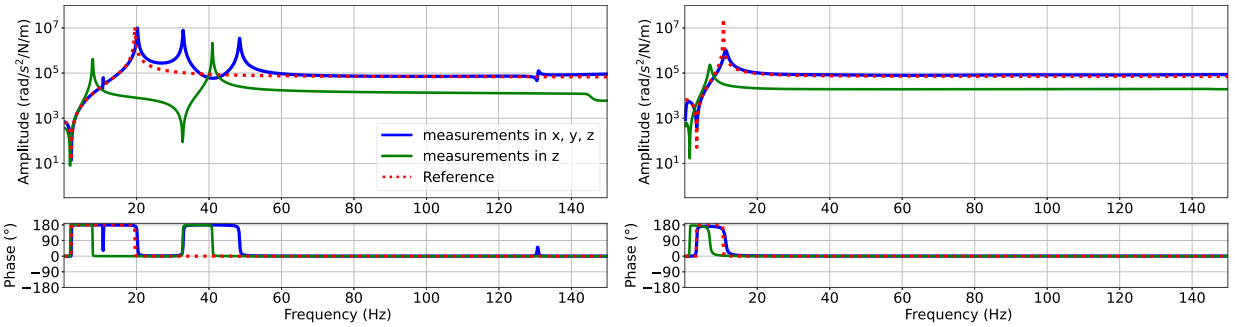

(a) Accelerance FRF at $q_{2\theta_x}$ (b) Accelerance FRF at $q_{2\theta_y}$

Fig. 11. Effect of the measured DoFs m on the solution. A pseudo-interface is used in the decoupling.

Fig. 11 are obtained using a pseudo-interface in the decoupling step. It can be noticed that when using the first set of measured DoFs, the natural frequencies of the joint at 11 Hz and 20 Hz, corresponding to its second and third modes of vibration in free–free conditions, are correctly estimated. Instead, when the second set of measured DoFs is used, the natural frequencies are not correctly estimated. In Table 1, the estimated physical parameters of the joint, obtained from these solutions as described in Section 4.1, are compared. The order of magnitude of the stiffness parameters of the joint is correctly estimated, whilst the moments of inertia of the joint are largely overestimated (more than one hundred times) when only measurements in the z direction are used. The reason is that measurements in the x and y directions carry information about the corresponding rigid body modes, which are needed to correctly identify the moments of inertia of the joint. However, it is important to note that performing measurements in the x and y directions for experimental identification is problematic due to the small thickness of the beams.

Table 1
Estimated mass and stiffness parameters of the joint at q_2. A pseudo-interface is used in the decoupling.

Solutions	m (kg)	I_{θ_x} (kg m^2)	I_{θ_y} (kg m^2)	K_z (N m^{-1})	K_{θ_x} (N m rad^{-1})	K_{θ_y} (N m rad^{-1})
Reference	0.12	1.49×10^{-5}	1.48×10^{-5}	139.03	0.219	0.05
Measurements in x, y, z	0.12	1.43×10^{-5}	1.42×10^{-5}	139.03	0.216	0.05
Measurements in z	0.12	2.00×10^{-3}	1.50×10^{-3}	138.95	0.290	0.05

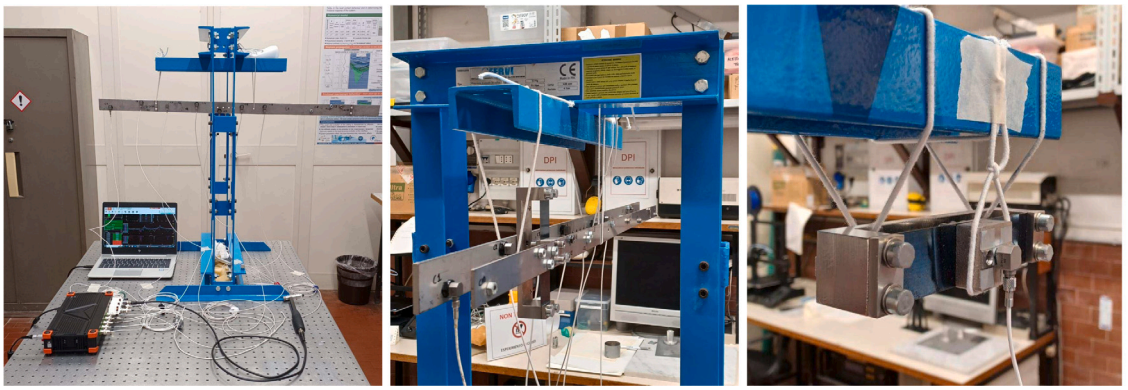

(a) Substructure A and experimental setup (b) Assembled structure (c) Joint substructure

Fig. 12. Experimental testing campaign: (a) residual substructure A; (b) assembled system AJB; (c) joint substructure J.

7. Experimental application

In this Section, the identification procedure is performed using experimental measurements of the benchmark structure introduced in Section 6.

The identification procedure requires the parent model of each beam to build its hybrid model, which is also used when generating the parent model of the assembled structure at each iteration. The parent models are generated as described in Section 6. The interface surfaces of each beam are modeled using two remote points with three DoFs, representing the coupling DoF set c: the translational DoF along the z axis and the two rotational DoFs around the x and y axis. The total number of coupling DoFs is $N_c = 6$. The same set of measured DoFs m and validation DoFs v used in the numerical application are selected on the structure. However, only DoFs in the z direction are considered because it is difficult to measure in the x and y directions due to the small thickness of the beams. Here, the number of measured DoFs m in the z direction is $N_m = 18$ (9 DoFs for each beam). One validation DoF v is selected on each beam. The mode superposition method is used to obtain the parent model FRFs of each beam on its global set of DoFs g ($g = m \cup v \cup c$).

7.1. Experimental setup

Here, the procedure to obtain the experimental model of the two beams and of the assembled system is described. Special care is taken during the measurements to apply low levels of excitation to the structures. This ensures that nonlinearities, which can be observed mainly in the joint, remain unexcited. The overlay models are defined on the set of measured DoFs m. Measurements are also performed to acquire the FRFs at the validation DoFs v. The single beams and the assembled structure are suspended through soft bungees to simulate free-floating conditions (Figs. 12(a) and 12(b)). Single-axis accelerometers (KISTLER 8776B250A) are used to measure accelerations. Impact excitations at each DoF are applied using a modal hammer (PCB 086C03). To obtain the FRF matrices, force and acceleration signals are acquired using the data acquisition system (SIRIUSi-DEWESOFT), based on DualCoreADC® technology with dual 24-bit delta-sigma analog to digital converter (ADC).

To validate the results of the experimental identification, the joint is also tested to obtain an experimental model (Fig. 12(c)). For this purpose, the joint is suspended with soft bungees to simulate free-free conditions. Only translational DoFs along the z axis are measured.

7.2. Results

In the following, the results of the experimental identification are analyzed. As discussed in Section 4.2, the conditioning of the IFM matrix improves if a pseudo-interface is used rather than an extended interface. The distribution of the normalized singular values σ_i/σ_1 of the IFM gives an indication of its conditioning: low values of this ratio suggest that the matrix is ill-conditioned. In Fig. 13, the normalized singular values distribution for the IFM at four frequencies is shown at the first iteration. It can be seen that

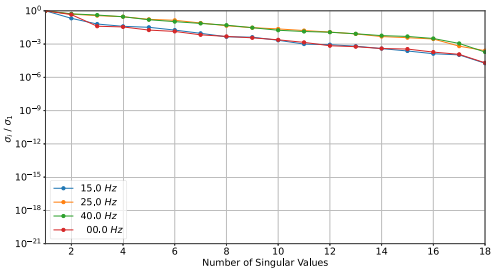

(a) Pseudo interface

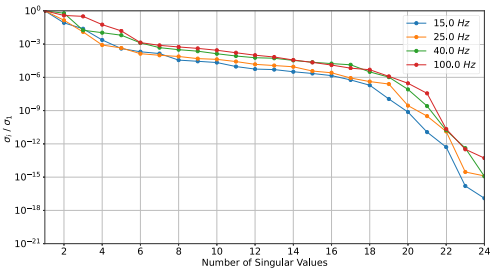

(b) Extended interface

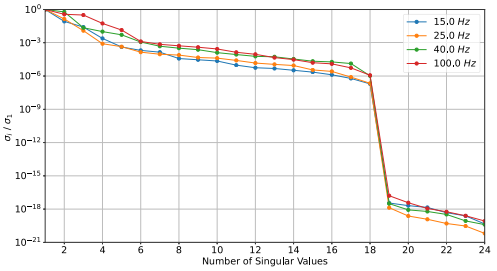

(c) Extended interface with weighting in SEMM expansion of RU ($w_{\mathrm{m}} = w_{\mathrm{v}} =$ 1e-8 and $w_{\mathrm{c}} = 1$)

Fig. 13. Normalized singular values distribution σ_i/σ_1 of the IFM at the first iteration when using an extended or pseudo-interface in the decoupling step.

the conditioning of the pseudo-interface (Fig. 13(a)) is better than the conditioning of the extended interface (Fig. 13(b)). Moreover, as seen in the numerical identification (Section 6), when an extended interface is used, a much higher weight should be assigned to the coupling DoFs c when performing the SEMM expansion on the assembled system to reach convergence. However, the used weights ($w_{\mathrm{m}} = w_{\mathrm{v}} =$ 1e−8 and $w_{\mathrm{c}} = 1$) cause a jump in the distribution of the normalized singular values of the IFM, shown in Fig. 13(c), since the last N_c singular values become negligible. Consequently, experimental error present in the data highly propagates in the solution. In this case, the strategy A proposed in Section 5.1.1 that truncates the last N_c singular values when inverting the IFM matrix, can be used to improve the solution. The three solutions' results are compared in Fig. 14. In particular, Figs. 14(a) and 14(b) show the driving point FRF and the dynamic stiffness of the joint at DoF q_{2z}, respectively. The red line represents the joint reference model obtained through experimental tests described in Section 7.1. The green line is obtained using the pseudo-interface in the decoupling step. The blue line is obtained using an extended interface and weights on the coupling DoFs in the SEMM expansion of RU ($w_{\mathrm{m}} = w_{\mathrm{v}} =$ 1e–8 and $w_{\mathrm{c}} = 1$). The orange line is obtained similarly to the blue line, but TSVD truncates the smallest N_c singular values in the inversion of the IFM matrix (strategy A). Note that the solution using the extended interface with no weights is not shown because it does not converge (as in the numerical case). It can be noticed from Fig. 14 that all these three solutions are affected by error propagation. However, the solution obtained using the extended interface and the weights in SEMM expansion (solid blue line) present spurious peaks higher than in the other solutions. Using the TSVD in the IFM (orange line) or the pseudo-interface (green line), the solution improves, particularly in the dynamic stiffness plot. Note that the orange and green solutions are overlapped. The coincidence between these two solutions can be explained by looking at Fig. 15, which shows the distribution of the singular values σ_i of the terms in Eqs. (29) and (26) at 25 Hz (the same behavior is observed at each frequency). The green curve refers to the $N_m = 18$ singular values of the IFM matrix for a pseudo-interface (no weights applied). The blue and yellow curves represent the $N_m + N_c = 24$ singular values of the whole IFM and of the second term in Eq. (26), respectively, for the extended interface and weights $w_{\mathrm{m}} = w_{\mathrm{v}} =$ 1e–8 and $w_{\mathrm{c}} = 1$ in the SEMM expansion of the assembled system. It can be noticed that the first 18 singular values of the blue and yellow curves coincide, and the last six are very small and similar. This confirms that when using the extended interface and weights, the sum of the first and third terms in Eq. (26) gives a negligible contribution to the IFM. As a consequence, since the rank of the second term of Eq. (26) is equal to N_m, also the IFM matrix has rank N_m. The truncation of the last N_c singular values correspond to consider only the difference $(\mathbf{Y}_{\mathrm{mm}}^{\mathrm{RU,ov}} - \mathbf{Y}_{\mathrm{mm}}^{\mathrm{R,ov}})$ that is for instance the expression of the IFM when using a pseudo-interface.

Since the reference model of the joint is generally not known, to validate the results, a comparison between the experimental FRFs of the assembled system and the FRFs of the system obtained by coupling the identified joint J with the model of the residual system R, can be performed at one of the validation DoFs v. In Fig. 16, this comparison is made for the validation DoF v_{1z} that belongs to beam A. It can be seen that the reconstructed FRFs obtained from results using the pseudo-interface and from results using the extended interface with strategy A, are in good agreement with the reference FRF up to 100 Hz, even though they are still prone to error propagation.

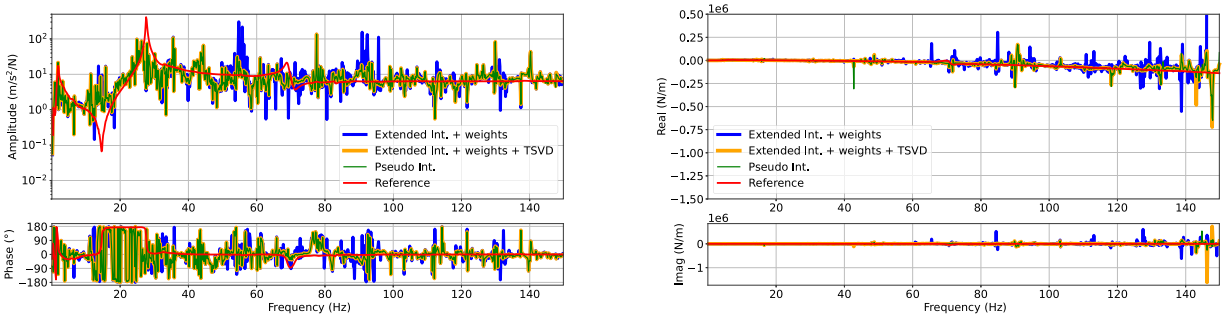

(a) Drive point FRF $\mathbf{Y}^{\mathrm{J}}$ at DoF q_{2z}

(b) Dynamic stiffness $\mathbf{Z}^{\mathrm{J}}$ at DoF q_{2z}

Fig. 14. Results of the experimental joint identification from different solutions; the reference models are obtained experimentally.

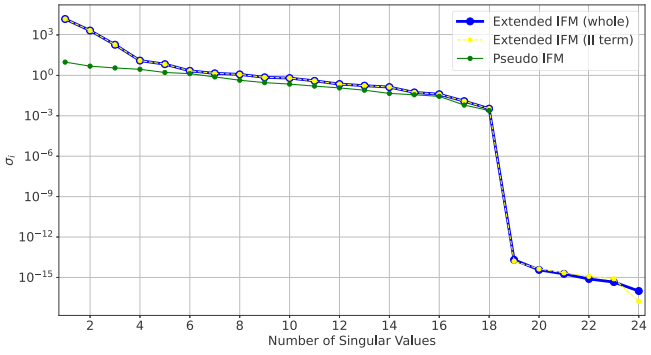

Fig. 15. Singular values distribution σ_i of the terms that give the interface flexibility matrix for the case of a pseudo-interface and for an extended interface (with weights in SEMM expansion of RU).

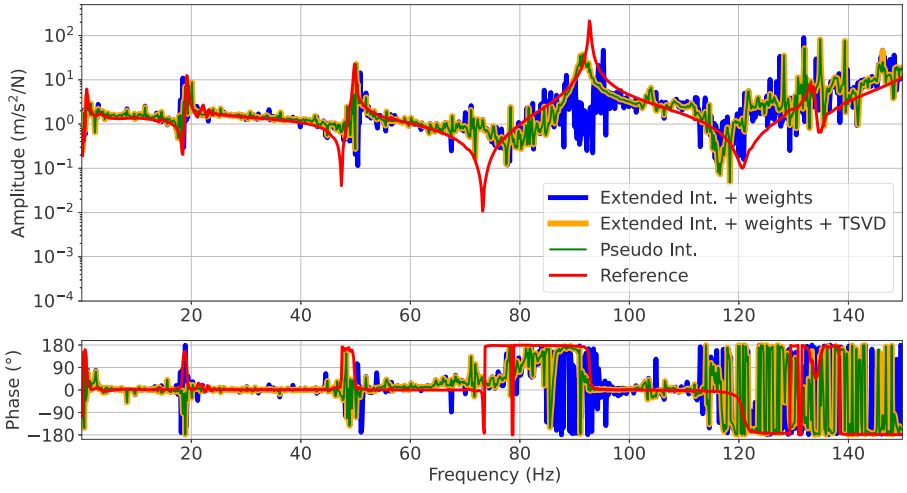

Fig. 16. Drive point FRF of assembled system at the DoF v_{1z} on beam A reconstructed with the identified joint.

To further improve the results, the fitting procedure proposed in Section 4.1 can be performed. The estimated joint FRFs $\mathbf{Y}^{\mathrm{J,est}}$ and the dynamic stiffness $\mathbf{Z}^{\mathrm{J,est}}$ obtained by the fitting procedure are compared in Fig. 17 with the reference model of the joint. In particular, the blue line refers to the joint model fitted from a solution in which weights are used, while the orange line is obtained by fitting the solution obtained using strategy A. It can be noticed that the use of the TSVD in the solution gives better results in terms of the estimated model of the joint. In fact, the TSVD reduces the spurious peaks in the identified dynamic stiffness, thus allowing more precise estimation of the joint parameters. The estimated model can be used also to reconstruct the dynamic behavior of the assembled system, as shown in Fig. 18. In this case, these reconstructed models are very similar, even though the corresponding

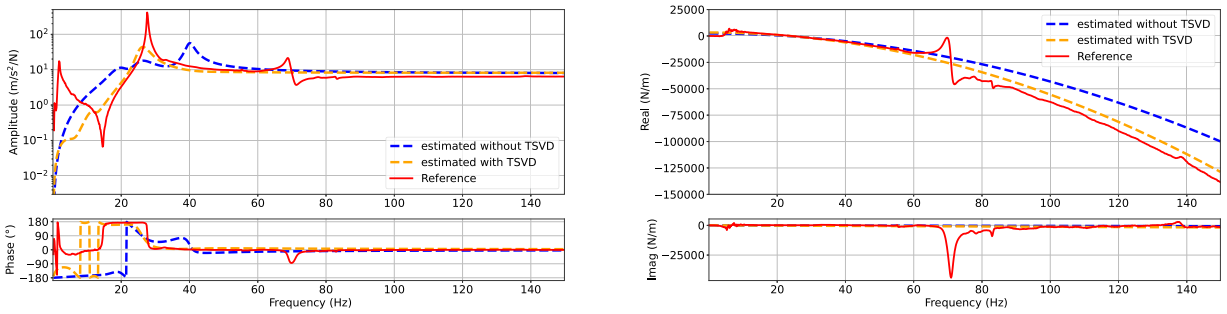

(a) Accelerance FRF (b) Dynamic Stiffness

Fig. 17. Results of the fitting on the solution: (a) drive point FRF $\mathbf{Y}^{\mathrm{J}}$ at DoF q_{2z}; (b) dynamic stiffness $\mathbf{Z}^{\mathrm{J}}$ at DoF q_{2z}. Weights $w_m = w_v = 1\mathrm{e}{-8}$ and $w_c = 1$ are used in SEMM expansion.

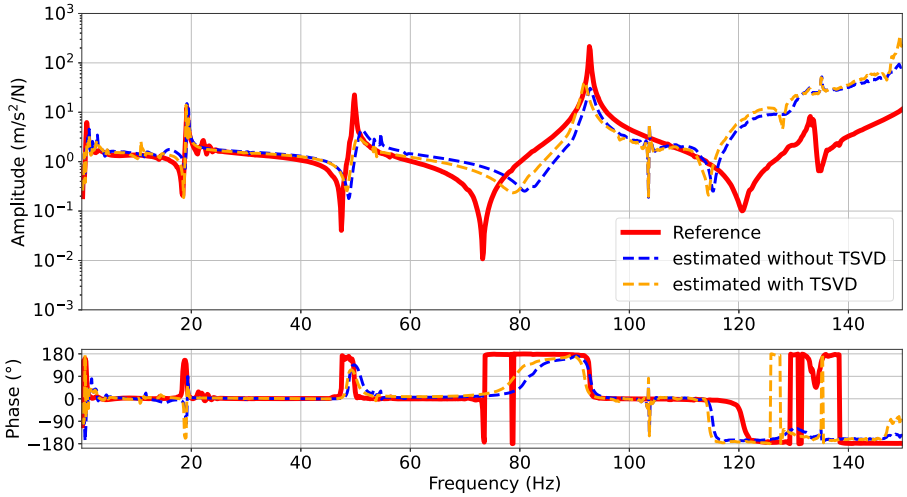

Fig. 18. Drive point FRF of the assembled system at DoF v_{1z} on beam A reconstructed with the joint FRF matrices $\mathbf{Y}^{\mathrm{J,est}}$: using the extended decoupling interface and weights in the SEMM expansion of the assembled system (blue curve); using strategy A (orange curve).

estimated joint models are considerably different. This may be due to the fact that the FRF of the assembly selected for validation is little sensitive to variation of the joint parameters in the selected frequency range. Thus the comparison of the reconstructed model is not so reliable in validating the results of the identification.

As suggested in Section 5.1.2, a different strategy can be adopted to improve the conditioning of the solution with the extended interface when weights are used. In this second strategy B, the TSVD is applied in the inversion of both the SEMM interface matrices in the expansion process on the assembled system and in the inversion of the IFM matrix. In all these three matrix inversions, only the first N_c singular values are retained. Fig. 19, shows the normalized singular values distribution at some frequencies for the matrices to be inverted in the SEMM expansion of RU, according to Eqs. (32) and (33). It can be noticed that a clear jump in the distribution of the normalized singular values arises at all frequencies. In particular, the first N_c singular values are more relevant than the other ones. Thus, the TSVD can be used when inverting these two matrices by retaining only the first N_c singular values. Consequently, this truncation also affects the normalized singular values distribution of the IFM matrix, shown in Fig. 20. In this case, in the IFM, only the first N_c singular values are relevant, while the remaining N_m must be truncated in the matrix inversion. The joint FRF $\mathbf{Y}^{\mathrm{J}}$ and dynamic stiffness $\mathbf{Z}^{\mathrm{J}}$ (blue lines) obtained by using strategy B are compared in Fig. 21 with the reference model of the joint (red curve). The green curves refer to the estimated joint accelerance $\mathbf{Y}^{\mathrm{J,est}}$ and dynamic stiffness $\mathbf{Z}^{\mathrm{J,est}}$, obtained by fitting the dynamic stiffness matrix $\mathbf{Z}^{J}$ from the solution using strategy B. It can be noticed that both the dynamics stiffnesses $\mathbf{Z}^{\mathrm{J}}$ and $\mathbf{Z}^{\mathrm{J,est}}$ are in good agreement with the reference joint model, and the spurious peaks are significantly reduced. Nonetheless, the identified joint FRF obtained using strategy B is less affected by error propagation, but it is not able to show the characteristics of its dynamic behavior. Instead, in the joint FRF $\mathbf{Y}^{\mathrm{J,est}}$ the resonance frequency at 36 Hz is well estimated, and the resonance frequency at 2.3 Hz is better estimated than the corresponding curve in Fig. 17. The reconstructed models of the assembled system obtained using the joint accelerances $\mathbf{Y}^{\mathrm{J}}$ and $\mathbf{Y}^{\mathrm{J,est}}$ are compared in Fig. 22 with the corresponding reference dynamic behavior, at the validation DoF v_{1z}. Compared to strategy A, strategy B avoids large error propagation in the solution, and the results are in really good agreement with the reference curve, up to 110 Hz.

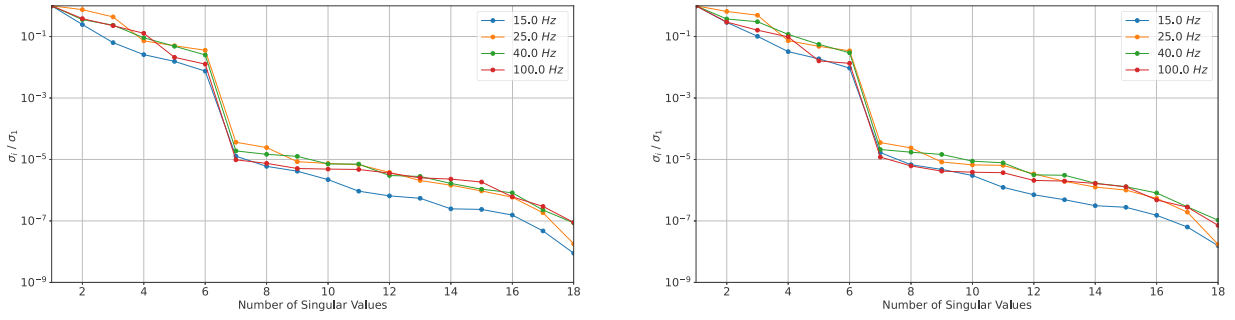

(a) $\mathbf{Y}_{\mathrm{mg}}^{\mathrm{AJB,par}}\mathbf{M}$ (b) $\mathbf{M}\mathbf{Y}_{\mathrm{gm}}^{\mathrm{AJB,par}}$

Fig. 19. Normalized singular values distribution σ_i/σ_1 at the first iteration, for the matrices to be inverted in the SEMM expansion of the assembled system when weights are used ($w_{\mathrm{m}} = w_{\mathrm{v}} = 1\mathrm{e}{-8}$ and $w_{\mathrm{c}} = 1$).

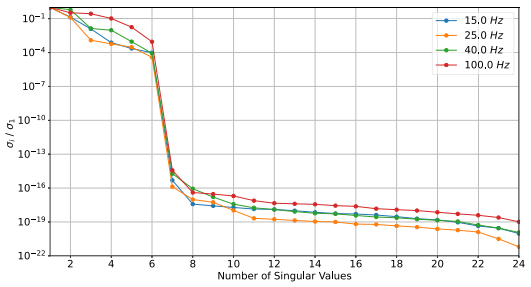

Fig. 20. Normalized singular values distribution σ_i/σ_1 of the IFM when strategy B is used.

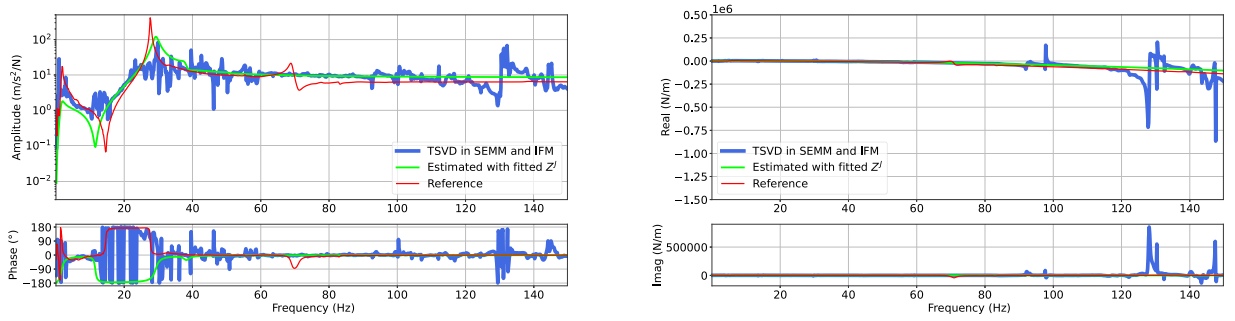

(a) Drive point FRF $\mathbf{Y}^{\mathrm{J}}$ at DoF q_{2z} (b) Dynamic stiffness $\mathbf{Z}^{\mathrm{J}}$ at DoF q_{2z}

Fig. 21. Results of the experimental joint identification using strategy B. The reference model is obtained experimentally.

8. Assessment of the different strategies using Monte Carlo simulation

This section aims to evaluate the effectiveness and robustness of the three strategies proposed in Sections 4.2 and 5 to improve the results of the SEMM-based identification procedure. As summarized in Table 2, the proposed strategies differ in several aspects, including the type of decoupling interface, the use of weighted pseudo-inverses in the SEMM expansion of the assembly, the use of TSVD in the inversions within SEMM, and the use of TSVD in the inversion within decoupling. The methodology used in [25] is also reported in Table 2, where no remedial actions are taken to reduce scatter in the solution. Due to the complexity of the problem, this study is carried out using the Monte Carlo approach [33], that can be used to analyze the propagation of uncertainties in the input variables of complex simulation-based models [34].

The uncertainty propagation of the iterative SEMM-based joint identification procedure is studied on the benchmark structure described in Fig. 6. The numerical models of the structure required for the Monte Carlo simulation are generated as described in Section 6.2. In this application, the inputs of the MC simulation are the overlay models $\mathbf{Y}^{\mathrm{A,ov}}$, $\mathbf{Y}^{\mathrm{B,ov}}$ and $\mathbf{Y}^{\mathrm{AJB,ov}}$ of the beam A, beam B and the assembled system AJB, respectively. The uncertainties are represented by the random noise that affects the FRF measurements of the overlay models. To simulate the presence of noise in the overlay model of a generic system s (with

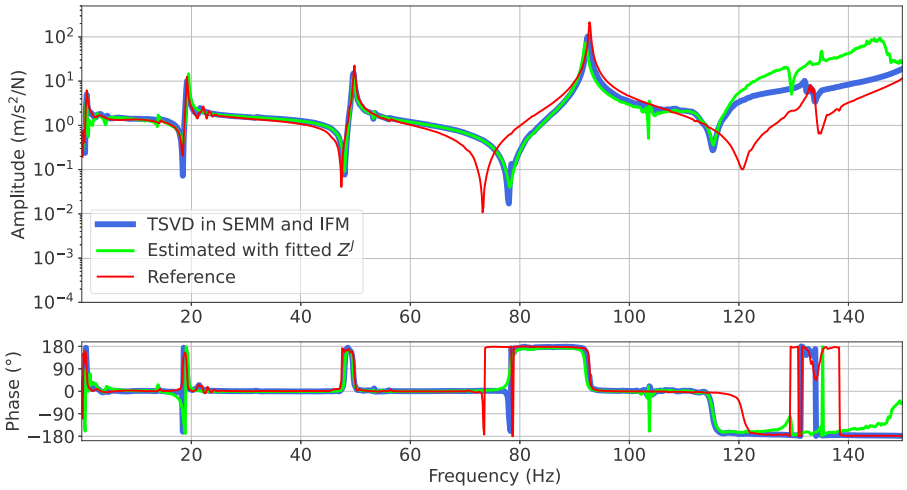

Fig. 22. Drive point FRF of assembled system at the DoF v_{1z} on beam A using strategy B.

Table 2
Possible strategies to improve the results of the SEMM-based joint identification procedure.

Strategy name	Decoupling interface	Weighs	TSVD in SEMM	TSVD in decoupling
Ref. [25]	Extended	Coupling DoFs	–	–
Pseudo	Pseudo	–	–	–
A	Extended	Coupling DoFs	–	N_m SVs retained
B	Extended	Coupling DoFs	N_c SVs retained	N_c SVs retained

$s = A,\ B,\ AJB$), a random perturbation is added to the numerically [16] simulated overlay FRF[3] $\hat{\mathbf{Y}}^{s,\mathrm{ov}}$:

$$Y_{ij}^{s,\mathrm{ov}}(\omega_k) = \hat{Y}_{ij}^{s,\mathrm{ov}}(\omega_k) + N_{ij}(\omega_k)E_{ij}p \tag{48}$$

where:

- $N_{ij}(\omega_k)$ is the Fourier transform of a band-limited white noise $n_{ij}(t)$ with zero mean and unit standard deviation, given by low-pass filtering a broad band white noise $w_{ij}(t)$, in the frequency band of interest;
- E_{ij} is the energy of the acceleration at DoF i to a unit excitation at DoF j, i.e. ($\hat{Y}_{ij}^{s,ov}$):

$$E_{ij} = \sum_{n=1}^{N_\omega} |\hat{Y}_{ij}^{s,\mathrm{ov}}(\omega_n)|^2 \frac{\Delta\omega}{2\pi} \tag{49}$$

  where N_ω is the number of the considered spectral lines and $\Delta\omega/2\pi$ is the frequency resolution;
- p represents the noise level, in this case selected as $p = 0.05$. This corresponds to 5% noise.

At the end of the Monte Carlo simulation, the statistical properties of the output joint accelerance FRF matrix are computed, in particular its mean value $\overline{\mathbf{Y}}^{\mathrm{J}}$ and standard deviation $\sigma(\mathbf{Y}^{\mathrm{J}}(\omega))$. A useful quantity to evaluate the effects of uncertainty propagation, is the confidence interval. For the FRF matrix of the joint, the confidence interval $\Delta(\mathbf{Y}^{\mathrm{J}}(\omega))$ can be expressed as:

$$\Delta(\mathbf{Y}^{\mathrm{J}}(\omega)) = 1.96\frac{\sigma(\mathbf{Y}^{\mathrm{J}}(\omega))}{\sqrt{N}} \tag{50}$$

According to Eq. (50), there is a 95% probability that a realization of the output FRF matrix of the joint lies between $[\overline{\mathbf{Y}}^{\mathrm{J}}(\omega) - \Delta(\mathbf{Y}^{\mathrm{J}}(\omega)), \overline{\mathbf{Y}}^{\mathrm{J}}(\omega) + \Delta(\mathbf{Y}^{\mathrm{J}}(\omega))]$.

Four different Monte Carlo simulations are performed according to the strategies defined in the Table 2. In each simulation, a number $N = 5000$ realizations[4] of $\mathbf{Y}^{\mathrm{A,ov}}$, $\mathbf{Y}^{\mathrm{B,ov}}$, and $\mathbf{Y}^{\mathrm{AJB,ov}}$ with different uncorrelated random errors are considered. These FRFs are computed at $N_\omega = 500$ frequency points. The results of the four Monte Carlo simulations are shown in Fig. 23 for the output joint accelerance FRF $q_{2z} - q_{2z}$. In particular, Fig. 23(a) shows the mean value of the joint accelerance obtained from each simulation. The reference FRF of the joint, obtained as described in Section 6.1, is also reported. It can be seen that when no strategy is used to

[3] The simulated noise-free FRFs are obtained using the mode superposition method.

[4] This number is selected such that the convergency of the Monte Carlo simulation is ensured.

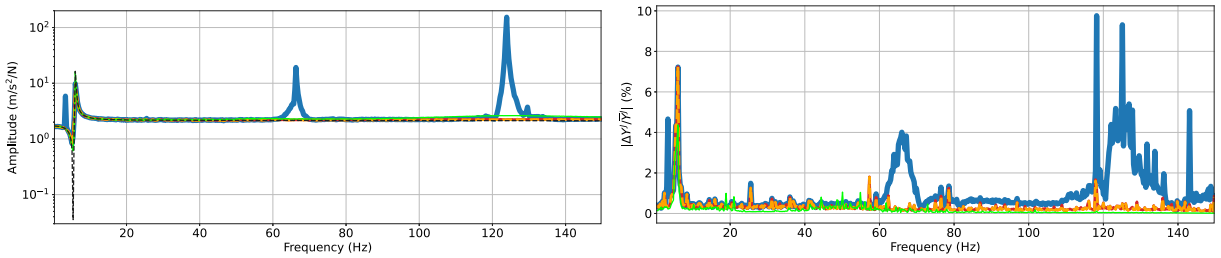

(a) Averaged FRF. (b) Relative Confidence Intervals.

Fig. 23. Statistical properties of the joint accelerance FRF $q_{2z} - q_{2z}$, obtained from four Monte Carlo simulations for the iterative SEMM-based joint identification procedure. In each simulation, except the blue curve, a different strategy is used to improve the results of the solution: (——) original solution from [25]; (——) pseudo-interface; (- - - -) strategy A; (——) strategy B; (- - - -) reference.

improve the solution (blue curve), additional spurious peaks appear in the joint FRF at 3.3 Hz, 66.3 Hz, 123.9 Hz and 129.6 Hz. Instead, all proposed strategies are able to correctly identify the joint FRF. More interesting is the plot of the relative confidence intervals for the joint FRF obtained from the Monte Carlo simulations, shown in Fig. 23(b). It is evident that the three proposed strategies are more robust to the presence of errors in the data, since these are less amplified by the iterative identification procedure. However, it is interesting to note that, apart from the spurious peaks at 3.3 Hz, the strategy using the decoupling pseudo-interface (red line) and strategy A (orange line) show the same performance in terms of error propagation in the case where no further action is taken (blue line), up to 40 Hz. At higher frequencies, however, the advantages of using these two techniques are significant. Moreover, Fig. 23(b) proves that the solution using the pseudo-interface in decoupling and strategy A coincide, as noted in Section 7.2. However, as shown in Fig. 23(b), strategy B gives the best performance in terms of error propagation. The FRF of the joint are predicted in this case with a relative confidence interval that, apart from the resonance of the joint, is lower than 1%.

9. Conclusions

In this paper, some improvements for an existing iterative joint identification technique, suitable for applications in which the joint interface is not measurable, are proposed. The focus is on the limitation of the error propagation in the procedure. The main sources of error propagation are localized in the matrix inversion present in the SEMM expansion (SEMM interface matrices) of the assembled system and in the decoupling step (Interface Flexibility Matrix). Two methods are proposed to improve the results of the identification:

- A fitting technique based on the identified joint dynamic stiffness matrix to smooth out spuriosity in the solution
- The use of a pseudo-interface (that only uses internal DoFs) in the decoupling step that avoids the propagation of the expansion error present on the coupling DoFs

The effectiveness of using a pseudo-interface is demonstrated with both numerical and experimental data.

Moreover, two strategies are proposed to improve the conditioning of the procedure when an extended interface is used since the weighting needed in the SEMM expansion of the assembled system to reach convergence makes the procedure ill-conditioned. Both strategies use the Truncated Singular Values Decomposition to perform matrix inversions in the SEMM expansion of the assembly and in the IFM. It is shown that the number of singular values to be retained depends on the number of coupling DoFs that are weighted. In the first strategy, the number of singular values neglected in inverting the IFM equals the number of coupling DoFs. In the second one, the number of singular values retained in inverting the SEMM interface matrices and the IFM is lower and equals the number of coupling DoFs. The effectiveness of the proposed strategies to reduce the error propagation in the procedure are experimentally verified on a benchmark structure and are also demonstrated using noisy polluted numerical data within a Monte Carlo approach.

Declaration of competing interest

The authors declare that they have no known competing financial interests or personal relationships that could have appeared to influence the work reported in this paper.

Data availability

Data will be made available on request.

Acknowledgments

This research is supported by University of Rome La Sapienza and University of L'Aquila.

Appendix. Generation of the parent model of the assembled system

The parent model of the assembled system RU can be generated by coupling the hybrid model $\mathbf{Y}^{\mathrm{R,hyb}}$ of the residual system R with the model $\mathbf{Y}^{\mathrm{J}}$ of the joint J obtained from the previous iteration. The coupling is performed using Eq. (7), in which:

$$\boldsymbol{u} = \begin{Bmatrix} \boldsymbol{u}_{\mathrm{m}}^{\mathrm{R}} \\ \boldsymbol{u}_{\mathrm{v}}^{\mathrm{R}} \\ \boldsymbol{u}_{\mathrm{c}}^{\mathrm{R}} \\ \boldsymbol{u}_{\mathrm{c}}^{\mathrm{J}} \end{Bmatrix}, \quad \mathbf{Y} = \begin{bmatrix} \mathbf{Y}^{\mathrm{R,hyb}} & \\ & \mathbf{Y}^{\mathrm{J}} \end{bmatrix} = \begin{bmatrix} \mathbf{Y}_{\mathrm{mm}}^{\mathrm{R,hyb}} & \mathbf{Y}_{\mathrm{mv}}^{\mathrm{R,hyb}} & \mathbf{Y}_{\mathrm{mc}}^{\mathrm{R,hyb}} & \\ \mathbf{Y}_{\mathrm{vm}}^{\mathrm{R,hyb}} & \mathbf{Y}_{\mathrm{vv}}^{\mathrm{R,hyb}} & \mathbf{Y}_{\mathrm{vc}}^{\mathrm{R,hyb}} & \\ \mathbf{Y}_{\mathrm{cm}}^{\mathrm{R,hyb}} & \mathbf{Y}_{\mathrm{cv}}^{\mathrm{R,hyb}} & \mathbf{Y}_{\mathrm{cc}}^{\mathrm{R,hyb}} & \\ & & & \mathbf{Y}_{\mathrm{cc}}^{\mathrm{J}} \end{bmatrix} \tag{51}$$

Differently from decoupling to couple two substructures, the compatibility and equilibrium conditions must be imposed at the coupling DoFs:

$$\boldsymbol{u}_{\mathrm{c}}^{\mathrm{R}} - \boldsymbol{u}_{\mathrm{c}}^{\mathrm{J}} = 0 \tag{52}$$

Eq. (52) can be written using the boolean matrix $\mathbf{B}$:

$$\mathbf{B} = \begin{bmatrix} \mathbf{0} & \mathbf{0} & \mathbf{I} & | & -\mathbf{I} \end{bmatrix} \tag{53}$$

Note that the result of the dual assembly in Eq. (7) has redundant DoFs since the coupling DoFs c appear twice. To remove this redundancy, one can use the localization matrix $\mathbf{L}$ that is the null space of $\mathbf{B}$:

$$\mathbf{Y} = \mathbf{L}^{+}\bar{\mathbf{Y}}(\mathbf{L}^{+})^{T} = \mathbf{L}^{+}\mathbf{Y}(\mathbf{L}^{+})^{T} - \mathbf{L}^{+}\mathbf{Y}\mathbf{B}^{T}(\mathbf{B}\mathbf{Y}\mathbf{B}^{T})^{-1}\mathbf{B}\mathbf{Y}(\mathbf{L}^{+})^{T} \tag{54}$$

With:

$$\mathbf{L} = \begin{bmatrix} \mathbf{I} & \mathbf{0} & \mathbf{0} \\ \mathbf{0} & \mathbf{I} & \mathbf{0} \\ \mathbf{0} & \mathbf{0} & \mathbf{I} \\ \mathbf{0} & \mathbf{0} & \mathbf{I} \end{bmatrix}, \quad \mathbf{L}^{+} = \begin{bmatrix} \mathbf{I} & \mathbf{0} & \mathbf{0} & \mathbf{0} \\ \mathbf{0} & \mathbf{I} & \mathbf{0} & \mathbf{0} \\ \mathbf{0} & \mathbf{0} & \mathbf{I} & \mathbf{0} \end{bmatrix} \tag{55}$$

By substituting Eqs. (51), (53) and (55) in Eq. (54), the expression for the parent model of the assembled system is obtained:

$$\mathbf{Y}^{\mathrm{RU,par}} = \begin{bmatrix} \mathbf{Y}_{\mathrm{mm}}^{\mathrm{R,hyb}} & \mathbf{Y}_{\mathrm{mv}}^{\mathrm{R,hyb}} & \mathbf{Y}_{\mathrm{mc}}^{\mathrm{R,hyb}} \\ \mathbf{Y}_{\mathrm{vm}}^{\mathrm{R,hyb}} & \mathbf{Y}_{\mathrm{vv}}^{\mathrm{R,hyb}} & \mathbf{Y}_{\mathrm{vc}}^{\mathrm{R,hyb}} \\ \mathbf{Y}_{\mathrm{cm}}^{\mathrm{R,hyb}} & \mathbf{Y}_{\mathrm{cv}}^{\mathrm{R,hyb}} & \mathbf{Y}_{\mathrm{cc}}^{\mathrm{R,hyb}} \end{bmatrix} - \begin{bmatrix} \mathbf{Y}_{\mathrm{mc}}^{\mathrm{R,hyb}} \\ \mathbf{Y}_{\mathrm{vc}}^{\mathrm{R,hyb}} \\ \mathbf{Y}_{\mathrm{cc}}^{\mathrm{R,hyb}} \end{bmatrix} (\mathbf{Y}_{\mathrm{cc}}^{\mathrm{R,hyb}} + \mathbf{Y}_{\mathrm{cc}}^{\mathrm{J}})^{-1} \begin{bmatrix} \mathbf{Y}_{\mathrm{cm}}^{\mathrm{R,hyb}} & \mathbf{Y}_{\mathrm{cv}}^{\mathrm{R,hyb}} & \mathbf{Y}_{\mathrm{cc}}^{\mathrm{R,hyb}} \end{bmatrix} \tag{56}$$

References

[1] Y. Ren, C.F. Beards, Identification of joint properties of a structure using FRF data, J. Sound Vib. 186 (4) (1995) 567–587, http://dx.doi.org/10.1006/jsvi.1995.0469.

[2] T. Yang, S.-H. Fan, C. Lin, Joint stiffness identification using FRF measurements, Comput. Struct. 81 (28) (2003) 2549–2556, http://dx.doi.org/10.1016/S0045-7949(03)00328-6.

[3] D. Čelič, M. Boltežar, Identification of the dynamic properties of joints using frequency–response functions, J. Sound Vib. 317 (1) (2008) 158–174, http://dx.doi.org/10.1016/j.jsv.2008.03.009.

[4] M. Wang, D. Wang, G. Zheng, Joint dynamic properties identification with partially measured frequency response function, Mech. Syst. Signal Process. 27 (2012) 499–512, http://dx.doi.org/10.1016/j.ymssp.2011.09.024.

[5] D. de Klerk, D.J. Rixen, S.N. Voormeeren, General framework for dynamic substructuring: History, review and classification of techniques, AIAA J. 46 (5) (2008) 1169–1181, http://dx.doi.org/10.2514/1.33274.

[6] D.-H. Lee, W.-S. Hwang, An identification method for joint structural parameters using an FRF-based substructuring method and an optimization technique, J. Mech. Sci. Technol. 21 (2007) 2011–2022, http://dx.doi.org/10.1007/BF03177459.

[7] M. Mehrpouya, E. Graham, S.S. Park, FRF based joint dynamics modeling and identification, Mech. Syst. Signal Process. 39 (1) (2013) 265–279, http://dx.doi.org/10.1016/j.ymssp.2013.03.022.

[8] S. Tol, H.N. Özgüven, Dynamic characterization of bolted joints using FRF decoupling and optimization, Mech. Syst. Signal Process. 54–55 (2015) 124–138, http://dx.doi.org/10.1016/j.ymssp.2014.08.005.

[9] M. Mehrpouya, M. Sanati, S.S. Park, Identification of joint dynamics in 3D structures through the inverse receptance coupling method, Int. J. Mech. Sci. 105 (2016) 135–145, http://dx.doi.org/10.1016/j.ijmecsci.2015.11.007.

[10] B. Jetmundsen, R.L. Bielawa, W.G. Flannelly, Generalized frequency domain substructure synthesis, J. Am. Helicopter Soc. 33 (1) (1988) 55–64, http://dx.doi.org/10.4050/JAHS.33.1.55.

[11] D. de Klerk, D.J. Rixen, J. de Jong, The frequency based substructuring (FBS) method reformulated according to the dual domain decomposition method, in: Proceedings of the 24th International Modal Analysis Conference, a Conference on Structural Dynamics, 2006, pp. 1–14.

[12] W. D'Ambrogio, A. Fregolent, Direct decoupling of substructures using primal and dual formulation, in: Linking Models and Experiments, in: Conference Proceedings of the Society for Experimental Mechanics Series, vol. 2, 2011, http://dx.doi.org/10.1007/978-1-4419-9305-2_5.

[13] S.N. Voormeeren, D.J. Rixen, A family of substructure decoupling techniques based on a dual assembly approach, Mech. Syst. Signal Process. 27 (2012) 379–396, http://dx.doi.org/10.1016/j.ymssp.2011.07.028.

[14] S.N. Voormeeren, D.J. Rixen, A dual approach to substructure decoupling techniques, in: Structural Dynamics, in: Conference Proceedings of the Society for Experimental Mechanics Series, 3, Springer, 2011, pp. 601–616, http://dx.doi.org/10.1007/978-1-4419-9834-7_53.

[15] W. D'Ambrogio, A. Fregolent, The role of interface DoFs in decoupling of substructures based on the dual domain decomposition, Mech. Syst. Signal Process. 24 (7) (2010) 2035–2048, http://dx.doi.org/10.1016/j.ymssp.2010.05.007.

[16] W. D'Ambrogio, A. Fregolent, Replacement of unobservable coupling DoFs in substructure decoupling, Mech. Syst. Signal Process. 95 (2017) 380–396, http://dx.doi.org/10.1016/j.ymssp.2017.03.038.
[17] W. D'Ambrogio, A. Fregolent, Substructure decoupling without using rotational DoFs: Fact or fiction? Mech. Syst. Signal Process. 72–73 (2016) 499–512, http://dx.doi.org/10.1016/j.ymssp.2015.11.029.
[18] M.V. van der Seijs, D. van den Bosch, D.J. Rixen, D. de Klerk, An improved methodology for the virtual point transformation of measured frequency response functions in dynamic substructuring, in: 4th ECCOMAS Thematic Conference on Computational Methods in Structural Dynamics and Earthquake Engineering (COMPDYN), Vol. 4, Greece, 2013, pp. 4334–4347, http://dx.doi.org/10.7712/120113.4816.C1539.
[19] E.A. Pasma, M.V. van der Seijs, S.W.B. Klaassen, M.W. van der Kooij, Frequency based substructuring with the virtual point transformation, flexible interface modes and a transmission simulator, in: Dynamics of Coupled Structures, in: Conference Proceedings of the Society for Experimental Mechanics Series, vol. 4, Springer, Cham, 2018, pp. 205–213.
[20] J.C. O'Callahan, P. Avitabile, R. Riemer, System Equivalent Reduction Expansion Process (SEREP), in: Proceedings of the 7th International Modal Analysis Conference, vol. 1, Society for Experimental Mechanics, Bethel, CT, 1989, pp. 29–37.
[21] L. Thibault, A. Butland, P. Avitabile, Variability improvement of key inaccurate node groups - VIKING, in: Topics in Modal Analysis II, in: Conference Proceedings of the Society for Experimental Mechanics Series, Vol. 6, Springer New York, New York, NY, 2012, pp. 603–624, http://dx.doi.org/10.1007/978-1-4614-2419-2_61.
[22] S.W.B. Klaassen, M.V. van der Seijs, D. de Klerk, System equivalent model mixing, Mech. Syst. Signal Process. 105 (2018) 90–112, http://dx.doi.org/10.1016/j.ymssp.2017.12.003.
[23] M. Pogačar, D. Ocepek, F. Trainotti, G. Čepon, M. Boltežar, System equivalent model mixing: A modal domain formulation, Mech. Syst. Signal Process. 177 (2022) 109239, http://dx.doi.org/10.1016/j.ymssp.2022.109239.
[24] S.W.B. Klaassen, D.J. Rixen, Using SEMM to identify the joint dynamics in multiple degrees of freedom without measuring interfaces, in: Dynamic Substructures, in: Conference Proceedings of the Society for Experimental Mechanics Series, 4, Springer, Cham, 2020, pp. 87–99, http://dx.doi.org/10.1007/978-3-030-12184-6_10.
[25] Z. Saeed, S.W.B. Klaassen, C.M. Firrone, T.M. Berruti, D.J. Rixen, Experimental joint identification using system equivalent model mixing in a bladed disk, J. Vib. Acoust. 142 (5) (2020) 1–29, http://dx.doi.org/10.1115/1.4047361.
[26] Z. Saeed, C.M. Firrone, T.M. Berruti, Joint identification through hybrid models improved by correlations, J. Sound Vib. 494 (2021) 115889, http://dx.doi.org/10.1016/j.jsv.2020.115889.
[27] L. Eldén, A weighted pseudoinverse, generalized singular values, and constrained least squares problems, BIT Numer. Math. 22 (4) (1982) 487–502, http://dx.doi.org/10.1007/BF01934412.
[28] S.W.B. Klaassen, D.J. Rixen, The inclusion of a singular-value based filter in SEMM, in: Proceedings of the 38th International Modal Analysis Conference, a Conference on Structural Dynamics, 2020.
[29] F. Latini, J. Brunetti, W. D'Ambrogio, A. Fregolent, Identification of normal modes of a set of strongly nonlinear springs, in: Materials Research Proceedings, in: 25th Conference of the Italian Association of Theoretical and Applied Mechanics, AIMETA 2022, vol. 26, 2023, pp. 443–448, http://dx.doi.org/10.21741/9781644902431-72.
[30] Ansys, Mechanical APDL Element Reference, ANSYS Inc, Release 2022 R2.
[31] Ansys, Mechanical APDL Theory Reference, ANSYS Inc, Release 2022 R2.
[32] T. Bregar, A. El Mahmoudi, M. Kodrič, D. Ocepek, F. Trainotti, M. Pogačar, M. Göldeli, G. Čepon, M. Boltežar, D.J. Rixen, pyFBS: A python package for frequency based substructuring, J. Open Source Softw. 7 (69) (2022) 3399, http://dx.doi.org/10.21105/joss.03399.
[33] N. Metropolis, S. Ulam, The Monte Carlo method, J. Amer. Statist. Assoc. 44 (247) (1949) 335–341.
[34] J. Zhang, Modern Monte Carlo methods for efficient uncertainty quantification and propagation: A survey, WIREs Comput. Statist. 13 (5) (2021) e1539, http://dx.doi.org/10.1002/wics.1539.